www.lpr-journal.org

LASER & PHOTONICS REVIEWS

WILEY-VCH

REPRINT

LASER
& PHOTONICS
REVIEWS

Laser Photonics Rev. **10,** No. 1, 13–39 (2016) / **DOI** 10.1002/lpor.201400467

Abstract Quantitative phase imaging (QPI), a method that precisely recovers the wavefront of an electromagnetic field scattered by a transparent, weakly scattering object, is a rapidly growing field of study. By solving the inverse scattering problem, the structure of the scattering object can be reconstructed from QPI data. In the past decade, 3D optical tomographic reconstruction methods based on QPI techniques to solve inverse scattering problems have made significant progress. In this review, we highlight a number of these advances and developments. In particular, we cover in depth Fourier transform light scattering (FTLS), optical diffraction tomography (ODT), and white-light diffraction tomography (WDT).

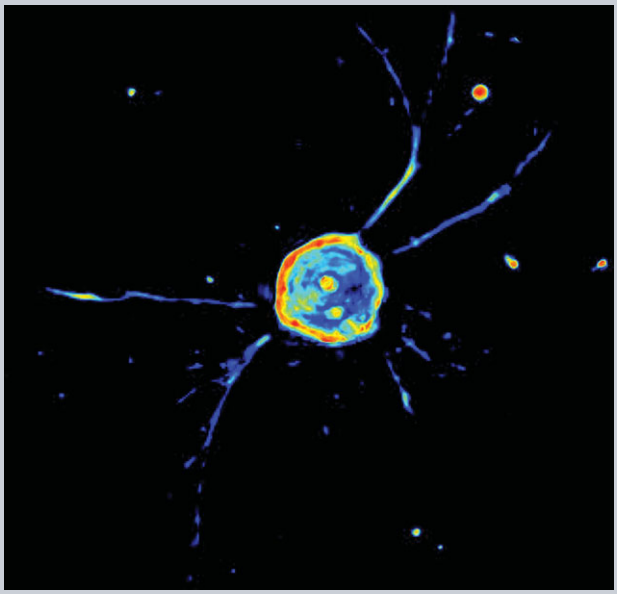

REVIEW
ARTICLE

Solving inverse scattering problems in biological samples by quantitative phase imaging

Taewoo Kim[1,], Renjie Zhou[1,2,3,**], Lynford L. Goddard[2], and Gabriel Popescu[1,*]**

1. Introduction

Light scattering is a basic interaction between an electromagnetic field and an inhomogeneous object, which results in modifications in the wavefront and field amplitude. If this interaction happens without modifications in the frequency, the scattering is said to be *elastic*. The scattered light carries the internal structural information of the object in its *amplitude* and *phase*. When the scattering through the object is weak, e.g., under the first-order Born approximation, the problem can be described as a linear process and, as a result, it is feasible to infer *uniquely* the object structure from the measured scattered field. This represents an *inverse scattering problem* and is fundamental to performing *tomographic imaging* of transparent structures such as live and unstained cells. An unstained live cell has features that are not only transparent, but also below the resolution of light microscopy. Moreover, the cell's internal structures, e.g., cytoskeleton, organelles, vesicles, are highly dynamic and, thus, difficult to study using labels. Therefore, reconstructing the three-dimensional (3D) structure of live, unlabelled samples has long been desired, which motivated the development of new tomographic imaging techniques using inverse scattering solutions.

Traditionally, inverse scattering methods are based on *far-zone* measurements, i.e., under the Fraunhofer approximation. For two-dimensional (2D) objects, such as apertures, diffraction gratings, etc., the far-zone measurement is directly related to the structure through a 2D Fourier transformation. However, in 3D inverse scattering, the problem becomes more complicated. There have been many attempts to solve 3D inverse scattering problems using far-field measurements. The first breakthrough was made by Bragg with X-ray diffraction [1], which is a method that has been widely used for determining crystal and crystalized protein structures [2,3]. However, it is well-known that in X-ray diffraction it is difficult to achieve experimental access to the phase of the field, i.e., the reconstruction suffers from non-uniqueness due to what became known as "the phase problem" [4]. In order to ameliorate the phase

[1] Quantitative Light Imaging Laboratory, Department of Electrical and Computer Engineering, Beckman Institute of Advanced Science and Technology, University of Illinois at Urbana-Champaign, Urbana, IL 61801, USA
[2] Photonic Systems Laboratory, Department of Electrical and Computer Engineering, Micro and Nanotechnology Laboratory, University of Illinois at Urbana-Champaign, Urbana, IL 61801, USA
[3] Laser Biomedical Research Center, G. R. Harrison Spectroscopy Laboratory, Massachusetts Institute of Technology, Cambridge, Massachusetts 02139, USA
**These authors contributed equally to this work
*Corresponding author: e-mail: gpopescu@illinois.edu

problem, prior knowledge about the structure of interest is used together with iterative methods, such that the reconstruction converges to an unambiguous solution.

Inspired by X-ray crystallography, in 1969, Wolf developed the theoretical formulation for tomographic imaging of *phase objects*, using monochromatic light to solve the inverse scattering problem. This method is known today as *optical diffraction tomography* (ODT) [5]. Recent reports successfully showed experimental demonstrations of ODT theory for 3D reconstruction of transparent objects. These experiments were commonly done by scanning the incident angle of the source beam by rotating either the source itself or the object, and measuring the scattering patterns in the far-zone [6–10]. This approach is based on laser illumination and, thus, suffers from laser speckle, which degrades the image contrast and resolution [11].

In 1991, *low-coherence interferometry* (LCI) was used for tissue imaging and the resulting method became *optical coherence tomography* (OCT) [13–15]. OCT images the sample at a depth position specified by the reference of the interferometer, with an axial resolution determined by the coherence length of the source rather than the numerical aperture of the imaging optics [16]. Usually OCT systems employ a low numerical aperture (NA) objective to maximize the imaging depth, and, thus, are limited to poor lateral resolution. The depth information is obtained by adjusting the delay of the reference field, while the transverse information is obtained by raster scanning. Importantly, the low temporal coherence in OCT is used to remove the scattered light outside the slice of interest, rather than to solve the inverse scattering problem. Common OCT systems perform intensity-based measurements of the backscattered light from various depths to gain information about the 3D object structure. Much later, in 2006, Ralston et al. developed a computational technique, called interferometric synthetic aperture microscopy (ISAM), to solve the inverse scattering problem by using the amplitude and phase of the OCT data. ISAM improves the lateral resolution and maintains it across the whole OCT imaging volume [14, 17, 18]. The inverse scattering problem was formulated based on diffraction tomography with the Green function approach.

Quantitative phase imaging (QPI) is an emerging field dedicated to providing a solution for the phase problem [19]. QPI combines holography proposed by Gabor in 1948 [20] and phase sensitive microscopy proposed by Zernike [21,22]. Instead of measuring the intensity of the total field, holography measures the interference between the scattered field and a reference field to record phase information. Further modifications to the reference field yields quantitative information about this phase difference at each point in space, and therefore, allows QPI techniques to measure the complex scattered field *quantitatively*. Moreover, recent advances in light sources and detectors have greatly benefitted imaging by providing sufficient pixel counts, high acquisition speed, and enough light sensitivity to acquire images needed for QPI applications. These advances have brought significant progress in solving the inverse problem in both 2D and 3D, by allowing one to work with the complex field itself rather than just the intensity [12, 14, 23–30]. This ability to precisely infer the 2D and 3D structures of a sample allowed QPI to be applied for many areas of studies, including biomedical imaging, material sciences, and more. However, in this review, we focus on solving inverse scattering problems of biomedical relevance.

In the early 2000's, A. Wax et al. pioneered the use of 2D inverse scattering theory with *angle-resolved low-coherence interferometry* (aLCI) to quantitatively characterize turbid structures [31–33]. In 2005, Alexandrov et al. used digital Fourier holography to measure the angular light scattering spectrum and reveal the object structure [34]. One of the earlier applications of QPI to inverse scattering problems was proposed by Ding et al. in 2008 [28]. This method, called *Fourier transform light scattering* (FTLS), can be thought of as the spatial equivalent of Fourier transform infrared (FTIR) spectroscopy. Analogous to FTIR, in which the spectroscopic information is obtained via a time-domain measurement followed by a numerical Fourier transformation, in FTLS the angular scattering (spatial frequency) information is obtained via a spatial-domain complex field measurement followed by a numerical Fourier transformation. Thus, measuring the quantitative phase image provides an ultrasensitive method for studying inhomogeneous and dynamic media [28, 35]. Initially, this technique was based on a QPI technique called *diffraction phase microscopy* (DPM), which measures the complex scattered field in a single shot [36]. Later, FTLS was expanded to other QPI methods, including white-light-based methods [37]. Since the technique is based on imaging instead of scattering measurements, all the scattering angles, or spatial frequencies, associated with the sample are measured simultaneously at each point of the image, which increases the sensitivity of the technique by orders of magnitude. Although this technique is confined to 2D measurements, it establishes the relation between quantitative phase imaging and light scattering [38,39]. Building on this principle, a new method, referred to as *dispersion-relation phase spectroscopy (DPS)*, was developed for studying dynamic transport of intracellular mass [40, 41].

3D inverse scattering based on optical diffraction tomography for biological imaging applications has been actively studied in the past decade. In early studies, filtered back-projecton methods, based on angle-scanning laser QPI, were used for 3D refractive index mapping [8, 10, 42]. Later on, Wolf's optical diffraction theory was applied to improve the resolution and the quality of 3D reconstruction [9,43]. In 2013, Y. Cotte et al. used a synthetic aperture laser QPI approach combined with the complex deconvolution of the system point spread function to achieve high resolution tomographic imaging [12]. Very recently, Kim et al. developed a new method of solving inverse scattering in the wavevector space and demonstrated the reconstruction of transparent objects in 3D [29]. This technique, referred to as *white-light diffraction tomography* (WDT), extends Wolf's diffraction tomography to broadband illumination and provides an accurate solution, without using the far-field approximation. Combined with a QPI technique called spatial light interference microscopy (SLIM) [26,44], WDT successfully reconstructed unlabelled live cells in 3D with

sub-micron resolution in all three directions. The wavevector space method used in WDT for solving the inverse scattering problems can also be used to solve many other problems, including inverse scattering using OCT [45].

As a result of this tremendous progress, we are at an exciting time in the Biomedical Optics field, where quantitative methods, typically reserved for material metrology, are suitable for studying live, unstained cells. Eight decades after Zernike's breakthrough that allowed us to "see" the internal structure of a completely transparent cell [21,22], we are now able to quantify the cell's size and 3D shape, how much dry mass it contains, how much light the cell scatters along particular directions, or quantify the diffusion coefficient of its internal structures.

In the following sections, we describe in more detail various approaches that use QPI to solve inverse scattering problems. The following sections are organized as follows. First, we review the basic principles of QPI (Section 2) and 2D inverse scattering methods including FTLS (Section 3). In Section 4 we review 3D inverse scattering methods and present representative results of live cell tomography. Finally, in Section 5 we summarize the results and project some exciting outcomes likely to occur in the coming years.

2. Quantitative phase imaging (QPI)

Since the 1990s, charge-coupled device (CCD) and complementary metal-oxide semiconductor (CMOS) based image sensors and personal computer technologies have made significant advancements, enabling *quantitative phase imaging* (*QPI*) to develop at a fast pace [19,46]. The megapixel resolutions of detectors yield sufficient details to be captured during imaging of nano-scale cellular structures. Moreover, the acquisition speed of these detectors can surpass one kHz, even when the full frame is used, thus allowing for the imaging of fast cellular dynamics. QPI, based on interferometric measurements, provides quantitative amplitude and phase information associated with the electromagnetic field. *Quantifying* the optical phase shifts associated with cells and tissues provides a new, valuable dimension to optical microscopy. Over the past decade, QPI has been recognized as an emerging area of research, as it enables previously inaccessible biological applications: cell dynamics [36, 47–53], cell growth [54–58], blood testing [51, 53, 56, 59–72], molecular detection [73] cell cytoplasm flow [74], heart cell beating [75], neuron imaging [76, 77], monitoring electric activity in nerves [78,79], cell and tissue refractometry [76,80,81], cell rheology [82,83] and, more recently, tomographic cell imaging [8, 10, 12, 27, 29, 42, 84]. Reference [85] reviews several major QPI technology breakthroughs in 2013.

Developments in QPI have brought significant progress in phase reconstruction, with phase sensitivity down to 1 mrad, corresponding to 1 nm thickness change, or conversely 10^{-4} refractive index change, in transparent biological structures (assuming a refractive index contrast of 0.03) [19, 40]. Importantly, QPI is a label-free method, without fluorescence markers or dyes, which keeps the specimen viable for extended periods of time. Therefore, it is ideal for biomedical imaging, where the live cells are sensitive to subtle perturbations in the environment [86–91]. Recently, various applications of QPI have been applied for non-invasive studies of cell dynamics, blood testing, cell growth, tissue diagnosis, and 3D cell imaging. Due to its non-destructive and high throughput nature, QPI has also been applied to material characterization [92–101].

Most QPI techniques are based on two-beam interferometry, in which a reference beam and a signal beam form an interference signal. In the general case of both spatial and temporal modulation, the measured intensity on the camera detector is

$$I(x,y;\tau) = I_{sig}(x,y) + I_{ref}(x,y) + 2\left|\Gamma_{12}(x,y;\tau)\right| \times \cos\left[\beta x + \omega\tau - \phi_{sig}(x,y)\right], \quad (2.1)$$

where $I_{sig}(x,y)$ and $I_{ref}(x,y)$ are the intensities of the signal and the reference beam, respectively, $\Gamma_{12}(x,y;\tau)$ is the cross-correlation between the reference and signal field, β is the spatial frequency shift between the two beams, ω is the mean temporal frequency of the two fields, τ is the temporal delay, and $\phi_{sig}(x,y)$ is the phase of the signal beam, i.e., the quantity of interest. There are two different interferometric techniques typically used to retrieve the signal field phase, $\phi_{sig}(x,y)$: *off-axis interferometry* and *phase-shifting interferometry*.

2.1. Off-axis QPI methods

In off-axis interferometry, the delay between the fields is minimized ($\tau = 0$) and the interference is recorded spatially. The angle between the two beams is non-zero, which creates a spatial frequency shift, β. Therefore, a fringe pattern is created with a period determined by the carrier frequency, β,

$$I(x,y;0) = I_{sig}(x,y) + I_{ref}(x,y) + 2\left|\Gamma_{12}(x,y;0)\right| \times \cos\left[\beta x + \phi_{ref} - \phi_{sig}(x,y)\right]. \quad (2.2)$$

Since the propagation of the two interference beams can be precisely described by diffraction theory, it allows for numerical reconstruction of the complex image field. In experiments, this type of interferometer is often realized in a Michelson or Mach-Zehnder interferometer, followed by a Hilbert transform of the acquired interferogram to recover the quantitative phase information ([59, 72, 86–102]).

In 1967, Goodman and Lawrence first demonstrated the numerical reconstruction of the complex field from a digitally recorded hologram. This approach has developed into a field of its own, known as digital holography [103]. Later on, Takeda et al. proposed a fast Fourier transform method to analyze the fringe pattern and reconstruct the sample topography [102]. As large CCD detector arrays became available in the 1990s, Schnars et al. demonstrated the first lens-less off-axis digital holography system with

improved image quality [87]. In the following years, digital holography was adapted in a microscopy system by several groups and became a new microscopic technique called digital holographic microscopy (DHM) [89, 104–107]. DHM is a scattering plane measurement, which requires deconvolution using the Fresnel propagation kernel to retrieve the complex field at the image plane. However, the optimum position of the detector to avoid spatial sampling and phase discontinuity problems in live cell imaging is at the image plane. In 2005, an off-axis QPI method called Hilbert phase microscopy (HPM) was proposed, in which the CCD camera is placed exactly at the image plane. HPM uses the complex analytic signal obtained from the measured intensity (which is real-valued) to retrieve the phase of a transparent object. Therefore, HPM is a single-shot technique, suitable for studying cell dynamics and morphology [59, 108, 109].

2.2. Phase shifting QPI methods

In phase-shifting interferometry, the angle between the reference and the scattered beam is zero ($\beta = 0$), while the reference field phase $\phi_{ref}(\tau)$ is modulated several times in order to obtain quantitative phase images. Therefore, Eq. (2.1) becomes,

$$I(x, y; \tau) = I_{sig}(x, y) + I_{ref}(x, y) + 2\left|\Gamma_{12}(x, y; \tau)\right| \cos\left[\phi_{ref}(\tau) - \phi_{sig}(x, y)\right]. \quad (2.3)$$

The reference phase $\phi_{ref}(\tau) = \omega\tau$ can be shifted by either changing the delay τ or the frequency ω of the light beam. By combining four interferograms taken at $\phi_{ref}(\tau) = 0,\ \pi/2,\ \pi,\ 3\pi/2$, the phase of the sample field is uniquely determined as,

$$\phi_{sig}(x, y) = \arg[I(x, y; 0) - I(x, y; \pi), I(x, y; 3\pi/2) - I(x, y; \pi/2)]. \quad (2.4)$$

In 1993, the group led by Graham Dunn at King's College, London, developed a technique called digitally recorded interference microscopy with automatic phase-shifting (DRIMAPS) based on a Mach-Zehnder interferometer setting [48, 110, 111]. In this technique, the phase shift is added to the reference by horizontally sliding an optical wedge. Another experimental setup was developed in 1998 at Northeastern University. This technique, called optical quadrature microscopy (OQM), is based on phase shifts generated by polarization waveplates. OQM was initially used to determine the sign of the Doppler velocity [112, 113], and later on applied to cell counting in embryos [114, 115]. More recently, several groups have developed QPI methods that simultaneously generate four phase shift images, which increased the acquisition speed and have enabled imaging of fast dynamics [116–119].

2.3. Common-path QPI methods

In 2004, a common-path phase-shifting QPI technique called Fourier phase microscopy (FPM) was developed [60, 120]. FPM uses a quasi-monochromatic source and phase-shifting interferometry to measure quantitatively the phase of transparent biological structures. In the first FPM demonstration, a super-luminescent diode (SLD) was used as illumination [60]. To ensure full spatial coherence on the CCD camera, the SLD is spatially filtered through a single mode fiber. A Fourier lens is used to separate the reference (transmitted) and signal (scattered) fields. The reference field is focused onto a spatial light modulator (SLM) where four phase shifts are created sequentially. The phase contrast images are captured at the image plane and used to reconstruct the phase map using Eq. (2.4). The phase shifting procedure allows for measuring the phase difference between the scattered and transmitted field. It should be pointed out that this phase difference, $\Delta\phi(x, y)$, is quite different from the phase associated with the image field, which is the coherent sum of the scattered and transmitted fields. The phase of the image field is calculated as,

$$\phi_{sig}(x, y) = \arg\{1 + \alpha(x, y)cos\left[\Delta\phi(x, y)\right], \alpha(x, y)\sin\left[\Delta\phi(x, y)\right]\}, \quad (2.5)$$

where $\alpha(x, y) = |E_{sig}(x, y)/E_{ref}(x, y)|$ and $E_{sig}(x, y)$ and $E_{ref}(x, y)$ are the electric fields of the signal and reference beams. FPM has high temporal stability, without the need for active stabilization. FPM has been used for measuring nanoscale membrane fluctuations and cell growth [55, 71].

In 2006, a new type of common-path off-axis transmission QPI method was developed called, *diffraction phase microscopy* (DPM) [36]. The first DPM was built using a laser illumination filtered through a single mode fiber to ensure full spatial coherence [28]. Using the laser as a light source, an image is formed through a commercial microscope at the image plane, where the DPM module is attached. The DPM module includes a $4f$ lens system that grants access to the Fourier plane of the field. A diffraction grating is placed at the microscope image plane to generate multiple diffraction orders. These diffraction orders are spatially separated in the Fourier plane, where a physical pinhole filter or an SLM is located. This filter low-passes the 0^{th} order diffracted beam to generate a reference beam and passes the 1^{st} order diffracted beam without filtering to carry the signal from the sample. These two beams are then combined at the image plane through the second Fourier lens to form an interferogram at the detector. Since these two beams are traveling in a common-path geometry, any noise induced by vibration of the optical elements is minimized, enabling optical path length sensitivity below 1 nm. Furthermore, DPM is a single-shot technique with the acquisition speed limited only by the acquisition rate of the camera. Therefore, this system is suitable for studying nanometer scale fluctuations in a highly dynamic sample. As an example, red blood cell membrane dynamics and other mechanical properties have been studied

using DPM [36, 40, 51, 121]. More recently, DPM has been extended to white-light illumination [122] and imaging samples in a reflection geometry [93–97]. Over the past several years, many other common-path QPI methods have also been proposed. For example, V. Mico et al. have demonstrated common-path QPI by spatial multiplexing the fields illuminated by three different illumination angles [123, 124]. Quadri-wave lateral shearing interferometry (QWLSI) [125] and spiral phase contrast [126] are also proposed as alternative common-path QPI methods.

Interestingly, over the past few years, QPI methods based on numerical computation have been widely explored. Phase and amplitude imaging based on the transport of intensity equation (TIE) is a computational QPI method based on the paraxial wave propagation. [127–130]. TIE involves measurements of light (coherent or partially coherent) intensity at two focal positions without using an interferometer and calculates the intensity axial derivative to obtain quantitative phase images. To reduce the noise and improve phase accuracy, Waller et al. proposed using higher-order derivatives that use three or more focal plane positions [128]. Fourier ptychographic microscopy [131] is a synthetic aperture technique in which the complex image field is reconstructed via individual spatial frequency components, measured sequentially. The scattering intensity corresponding to each **k**-vector is collected via a low NA objective and both the amplitude and phase information of the field are recovered by using an iterative computation method. This method can achieve a large field of view with moderate lateral resolution, thus, significantly improving the spatial bandwidth product. However, the imaging speed and the source brightness remain as problems that prevent Fourier Ptychographic Microscopy (FPM) from real-time imaging. Gerchberg-Saxton (G-S) algorithm [132] is another widely used iterative phase-retrieval method. For more references, the Fienup group has done extensive work on iterative phase-retrieval algorithms [133].

2.4. White-light QPI methods

2.4.1. wDPM and wFPM

Laser based QPI techniques suffer from laser speckle, due to the high coherence of the laser, which degrades the image quality. To mitigate this problem, several white-light QPI techniques have been developed recently. In 2012, Bhaduri et al. developed a white-light version of DPM (wDPM) [122, 134]. In wDPM, an SLM is used as the spatial Fourier filter to ensure full coherence of the reference field at the CCD camera. wDPM significantly improves spatial and temporal sensitivity over laser DPM and has been used for studying cell morphology and dynamics [122]. To follow up with this white-light method, Edwards et al. and Nguyen et al. studied the spatial coherence properties in wDPM for optimizing the method [135, 136]. In 2013, a white-light version of FPM (wFPM) was also developed and used to study cell membrane dynamics [120].

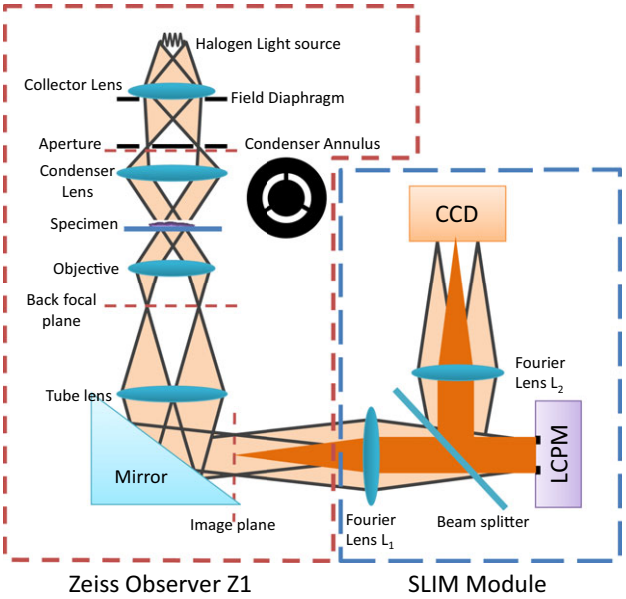

Figure 1 Spatial light interference microscopy setup.

2.4.2. Spatial light interference microscopy (SLIM)

In 2011, a white-light phase-shifting QPI method, called spatial light interference microscopy (SLIM), was demonstrated [137]. SLIM is an add-on to a commercial phase-contrast microscope with a white-light illumination generated by a halogen lamp and filtered by a ring-shaped annulus. In SLIM, as illustrated in Fig. 1, the back focal plane of the phase contrast objective lens is relayed to the Fourier plane of the 4*f* lens system, located at the output port of a commercial microscope. At this plane, a spatial light modulator (SLM) or a liquid crystal phase modulator (LCPM) adds four different phase delays, 0, $\pi/2$, π and $3\pi/2$, to the reference field, generating four different interferograms at the detector plane. Combining these four interferograms, the phase delay through the objective can be reconstructed according to Eqs. (2.4) and (2.5).

Since SLIM is based on a commercial microscope, it can utilize all the microscope peripherals such as atmosphere control, temperature control, or high-precision stages. Furthermore, due to the low-coherence illumination and the common-path geometry, SLIM ensures high temporal and spatial sensitivities, 0.03 nm and 0.3 nm in optical path length, respectively [44]. Therefore, with this high sensitivity and stability, SLIM is suitable for imaging unlabelled live cells for a long period of time, as the cell growth happens over days and the changes in mass are on the scale of picograms [138, 139]. Needless to say, it can also be coupled with other microscopy modalities, such as fluorescence microscopy, to obtain more specific information about the sample. Recently, a SLIM system has been improved in its speed to acquire 12.5 phase images per second, making it suitable for fast dynamics studies [50].

Another advantage of SLIM is the inherent depth sectioning effect due to the low-coherence illumination.

Table 1 Characteristic attributes of QPI techniques

Technique	Attribute
Off-axis	High speed
Phase-shifting	Wide field of view
Common-path	High temporal sensitivity
White-light	High spatial sensitivity

Similar to OCT, the coherence gating effect makes it suitable for 3D tomographic reconstruction of the sample refractive index distribution. Wang et al. have shown that SLIM is capable of imaging live cells in 3D with axial resolution of 1.34 μm [26]. Studies by Mir et al. have shown that, with a sparsity constraint based deconvolution, SLIM reconstructs the helical sub-cellular structures in *Escherichia coli (E. coli)* cells [27]. Building upon these experimental results, Kim et al. have developed a physical model to describe the 3D imaging principle of SLIM system, by extending Emil Wolf's diffraction tomography to a broad-band source, and further improved the tomographic imaging using SLIM [5, 85]. This result is described in detail in Section 4.4.

2.5. Summary

In summary, each technique applied for QPI provides a unique advantage to the imaging technique. Off-axis techniques are fast due to their single-shot nature. Phase-shifting techniques maintain a wide field of view and diffraction limited resolution (large space-bandwidth product), since they do not require additional magnification. Common-path techniques have high temporal sensitivity due to their insensitivity to any time-varying noise such as vibrational noise. White-light techniques are speckle free and offer excellent spatial sensitivity due to their low temporal coherence. QPI techniques can be categorized by these four attributes as shown in Table 1. Hybrid QPI techniques have been developed to include as many of these benefits as possible. For example, wDPM is an off-axis, common-path, white-light technique, and SLIM is a phase-shifting, common-path, and white-light technique. One possible way to combine all the benefits of these QPI methods would be to simultaneously generating and capturing the multiple frames of a phase-shifting interferometry based QPI system with a white light source. In fact, a similar approach has already been demonstrated [116, 140].

Recent advances in this field of study have brought many different QPI techniques to provide highly sensitive phase measurement in both 2D and 3D, with diffraction limited resolution. Since QPI grants information about the complex field, inverse scattering problems can be solved, and consequently, tomographic reconstruction of transparent objects is possible. In the following sections, several inverse scattering techniques for inferring the object structure from QPI measurements will be discussed in detail.

3. Two-dimensional inverse scattering

With the recent advances of imaging detectors, light scattering measurement techniques have also been advanced toward broader spatiotemporal scales of investigation, higher sensitivities and higher throughput [70, 141–144]. Recent developments in QPI have enabled quantitative measurements of the complex field and direct extraction of the refractive index of cells and tissues [36, 44, 59, 81, 109]. Under the first-order Born approximation, the measured imaging field can be translated into the angular scattering signal via a Fourier transform [145], giving light scattering information from all measurable spatial scales. Therefore, the scattering object can be defined uniquely by solving the inverse scattering problem in 2D.

3.1. Angle-resolved low coherence interferometry (aLCI)

An example of early approaches of 2D inverse scattering is angle-resolved low coherence interferometry (aLCI). Wax et al., using a modified Michelson (Linnik) interferometer, measured the angular distributions of backscattered light from a turbid media [31, 32]. In this system, the Fourier lens leading to the reference arm is translated perpendicular to the optical axis, introducing a shift to the reference ray, and thus, shift in the incident wave angle at the detector. Therefore, the detector measures the cross-correlation between the reference and the plane wave component of the scattered field that corresponds to the angle of the reference beam. By scanning the angle, the angular distribution of the scattered light is measured. Using this angular distribution, 2D samples are characterized, and further, using the low coherence source, the technique is extended to perform depth-resolved imaging [146]. aLCI has been used for characterizing the structure and dynamics of live biological cells without labeling as well as for medical imaging of tissue samples for diagnosis [147–151]. More recently, fiber-optic based aLCI for *in vivo* clinical applications has been demonstrated by Zhu et al. [152, 153]. As shown in Fig. 2, the authors applied the fiber-optic aLCI system to measure the nuclear morphology *in vivo*. This technique was used for detection of dysplasia in Barrett's esophagus as demonstrated in Terry et al. [154].

3.2. Synthetic aperture Fourier holographic optical microscopy

In 2005 and 2006, Alexandrov et al. showed that the angular light scattering spectrum and also the object structure at microscopic scale can be recorded by using digital Fourier holography [25,34]. The off-axis digital holography setup based on a Mach-Zehnder interferometer in the back scattering geometry forms a Fourier plane image at the CCD. Interference between the reference and the back scattered field at 2.3° angle forms a Fourier hologram with a

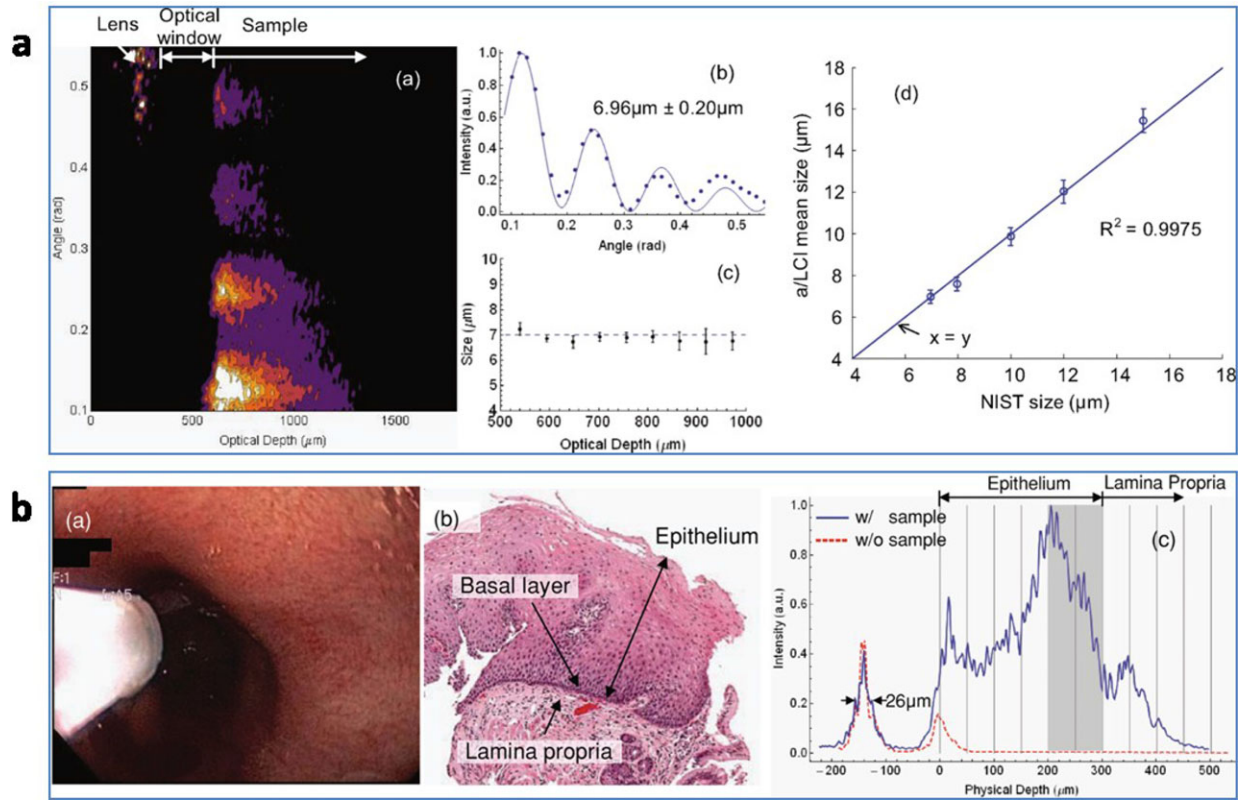

Figure 2 Demonstrations of fiber-optic aLCI. (a) Depth-resolved fiber-optic aLCI applied a distribution of 7 μm microspheres accompanied with Mie theory fit and sizing results. Measurement for beads of various sizes have also been demonstrated. (b) in vivo application of depth-resolved fiber-optic aLCI applied for human esophagus, accompanied with H&E microscopy image of the squamocolumnar junction and the depth profiles from the aLCI measurement. The figures are adapted from reference [153] with permission.

modulation spatial frequency of 60 cycles/mm. By masking the Fourier hologram to select only a scattering angle range of 1.2°, the scattered power is determined as a function of scattering angle. The Fourier hologram is then inverse Fourier transformed to reconstruct the image of the sample. An area corresponding to a microbead is selected and its scattering pattern is shown and compared with Mie theory, showing a good match between the theory and the measurement. This approach has been referred to as *synthetic aperture Fourier holographic optical microscopy* as it uses a frequency domain measurement to infer a high-resolution image.

3.3. Fourier transform light scattering (FTLS)

Fourier transform light scattering (FTLS) is a method for studying both static and dynamic light scattering [28], combining the high spatial resolution in optical microscopy and the intrinsic averaging of light scattering. FTLS is in some ways the reverse of the synthetic aperture Fourier holographic method, as it uses image plane measurements to extract scattering information. As illustrated in Fig. 3, *imaging* can be interpreted as the coherent summation (*interference*) of all the plane waves *scattered* by the object and captured via the numerical aperture of the imaging system (imaging = scattering + interference). Therefore, given that both the amplitude and phase information are obtained through imaging, the scattering from all angles can be recovered simultaneously, in one shot. In order to obtain amplitude and phase measurement, FTLS relies on the phase measurement of QPI techniques. The phase and amplitude associated with a microscope image, and, thus the information on the full complex field, is numerically propagated to the Fourier plane of the optical system, where the scattering distribution, $\tilde{U}(p_x, p_y)$, can be determined as,

$$\tilde{U}(\mathbf{p}_\perp, t) = \int U(\mathbf{r}_\perp, t) e^{i\mathbf{p}\cdot\mathbf{r}_\perp} dx dy. \qquad (3.1)$$

where $\mathbf{p} = \mathbf{k_s} - \mathbf{k_i}$ is the momentum transfer, $\mathbf{k_s}$ the scattered wavevector, $\mathbf{k_i}$ the incident wavevector and $\mathbf{r}_\perp = (x, y)$. Now, p, the magnitude of vector $\mathbf{p}$, is related to the scattering angle, θ, as $p = (4\pi/\lambda)\sin(\theta/2)$, where λ is the wavelength of the illumination. Therefore, the angularly scattered field, $\tilde{U}(\theta)$, can be determined from a single image through FTLS.

Validation of this technique was done by measuring polystyrene microbeads and comparing the scattering pattern with the Mie theory model for spherical scatterers [28]. After validating the technique, Ding et al. applied FTLS to

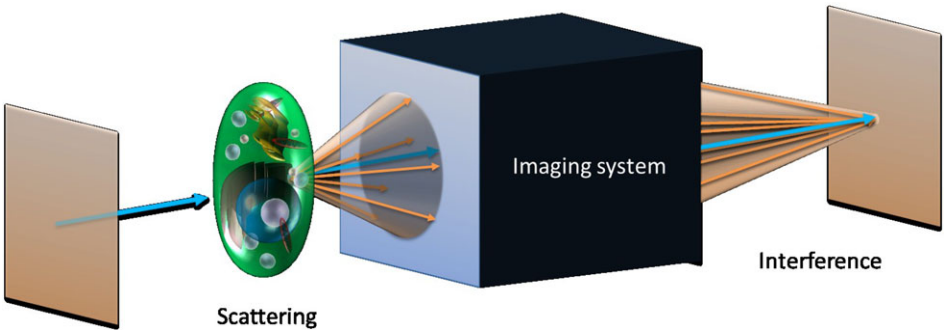

Figure 3 Imaging interpreted as an interference phenomenon between the unscattered field (blue arrow) and the scattered field (orange arrows).

extract scattering parameters, such as the anisotropy factor and the scattering mean free path, of biological tissue samples to characterize the bulk tissues [155]. Further studies showed that these scattering parameters can successfully separate the benign and cancerous regions in a prostate tissue biopsy [137].

Figure 4 shows an example of an FTLS measurement. Figure 4a shows the phase image of a human neuron culture obtained by SLIM. The scattered field in the spatial frequency domain is obtained by taking the Fourier transform of the complex image field. Figure 4b shows the amplitude distribution of the scattered field in the spatial frequency domain. Figure 4c shows the angular scattering signal obtained by averaging in the azimuthal direction of the map in Fig. 4b. Furthermore, the area marked with a dashed box in Fig. 4a is expanded and displayed in Fig. 4d, to show the scattering map of an FTLS result from an anisotropic sample. Figure 4e shows the scattering map, its elliptical shape indicating strong anisotropy. Figure 4f shows the profiles taken from the two angles indicated in Fig. 4e. The result demonstrates a much slower decay in the 20° direction, which is perpendicular to the dendrite structure in Fig. 4d, compared to the 110° direction. Also, the 20° profile shows a periodic ripple corresponding to the width of the dendrite. It important to emphasize that even though the scattering structure is very thin (dendrite portions in Fig. 4d), FTLS yields angular scattering intensity distribution with a dynamic range of over 3 orders of magnitude. A direct, goniometer-based measurement will likely require photon counting detection. The reason FTLS is so sensitive and of high dynamic range is that the measurement is performed at the image plane where all the **k-**vectors overlap, thus increasing the detected signal.

Recent developments of fast QPI systems, such as DPM or SLIM, enabled the acquisition of phase images at video rate [50, 134]. This high acquisition speed makes FTLS very suitable for studying fast dynamics. In order to quantify the dynamics of samples using the angular scattering signal from FTLS, human red blood cell (RBC) membrane fluctuations were studied [23, 28]. By taking time-lapse images of an RBC, the membrane displacement histogram and the power spectrum associated with the FTLS signal were calculated. The power spectrum showed different power laws with different exponents in time for all scattering angles. More specifically, the decay of the power spectrum was slower at larger angle (associated with smaller spatial dimension), indicating a more solid behavior. The exponent, -1.36, of the power spectrum at smaller angle matched with the exponent, -1.33, from a previous study done by Brochard et al. [156]. Furthermore, FTLS has been used to study the dynamic properties of Enteric glial cytoskeleton before and after treatment with Cytochalasin-D, which inhibits actin polymerization [157, 158]. Spatially averaged power spectra associated with FTLS signal for a single cell revealed that the membrane fluctuation on the untreated cell is more active. Also, frequency-averaged power spectra showed enhanced membrane fluctuation on the untreated cell. Comparing the power spectra before and after the treatment, it was shown that the disruption of actin contributes to more "random" or Brownian motion on the cell, as expected.

Further studies have advanced this type of imaging-based angular scattering studies and successfully quantified the dynamics of samples. By measuring the dispersion curves that depend on the temporal bandwidth at each spatial frequency, Wang et al. quantified dynamics, both random and deterministic, of intracellular transport using the quantitative phase images from a SLIM system [44]. Using the so-called *dispersion-relation phase spectroscopy* (DPS) technique, the authors have shown that the intracellular transport is dominated by diffusion, or Brownian motion, at small scale, and by directed motion at larger scale. Also, diffusion coefficients and transport velocities of these motions are extracted from the DPS technique.

More recently, FTLS has been combined with other means of optical techniques, such as angle-resolved scattering, swept-source spectroscopy and synthetic aperture. By combining with angle-resolved scattering methods, in 2012 and 2014, FTLS has been applied for studying red blood cells and individual rod-based bacteria by Kim et al. and Jo et al. [159, 160]. Application of FTLS has also been expanded for materials research by Yu et al. in 2012 [161]. The authors studied colloidal clusters using FTLS, and identified the scattering patterns of two-dimensional colloidal clusters including dimer, trimer and tetrahedron shapes. Furthermore, combining FTLS with swept-source spectroscopy and angle-resolved light scattering, Jung et al. added a new dimension to the FTLS measurements, now including the temporal frequency domain [162]. There has also been an attempt to simplify FTLS measurement by employing in-line geometry in the holographic measurement. In 2012, Kim et al. used an in-line holography geometry

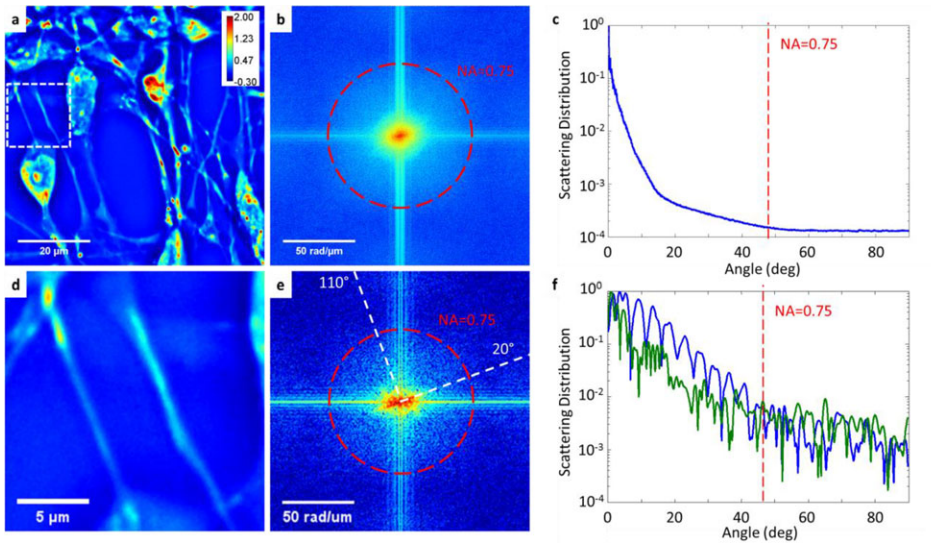

Figure 4 Fourier transform light scattering. (a) A quantitative phase image of a neuron culture acquired using SLIM. Color bar is in radians. (b) Scattering map calculated from the quantitative phase image. (c) Angular scattering signal acquired by radially averaging the scattering map. (d) A zoom-in from the area indicated in (a). (e) Scattering map calculated from the area shown in (d). (f) Angular scattering signals showing two perpendicular directions indicated in (e).

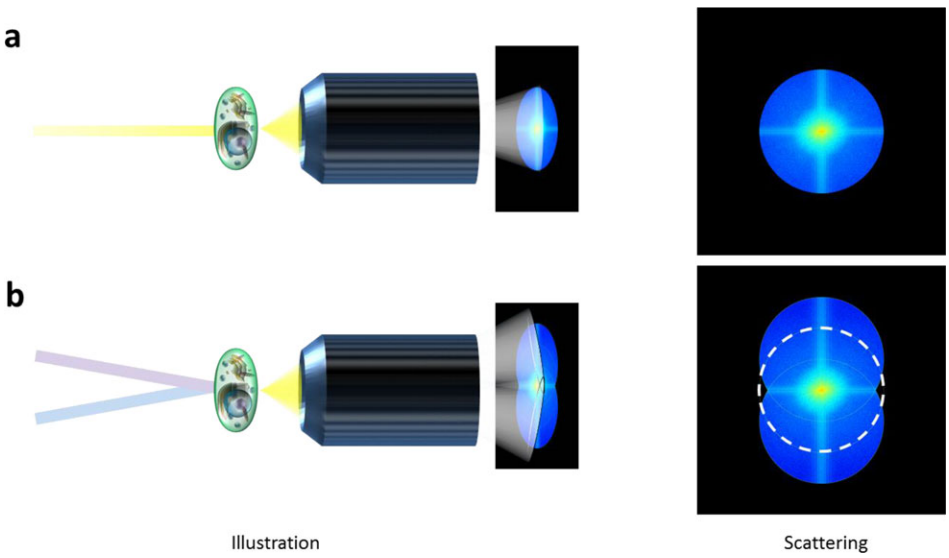

Figure 5 Illustration of synthetic FTLS. (a) Regular FTLS where the spatial frequency coverage is limited to the NA of the objective. (b) Synthetic FTLS where the spatial frequency is expanded.

and successfully applied FTLS measurement to the system [163]. One of the most significant improvement to FTLS has been demonstrated by Lee et al., in 2013 [164]. The authors applied the synthetic aperture technique to FTLS in order to expand the spatial frequency coverage beyond the NA of the objective. Figure 5 shows an illustration of the expanded spatial frequency coverage of synthetic FTLS.

3.4. Summary

Quantitative phase imaging, by providing the information about the complex field scattered by the object, directly relates light scattering measurements with imaging. Therefore, it is possible to infer the structure of the scattering object from the scattering measurements, such as aLCI and synthetic aperture Fourier holographic optical microscopy, by solving the inverse scattering problems in 2D. As shown with FTLS, it is also possible to obtain scattering information from a QPI image and infer the structural information from the spatial power spectrum. Furthermore, as shown in DPS, time-resolved QPI allows for measuring dynamic samples and obtain physical constants, such as diffusion coefficients and transport velocities. Further recent developments in 2D inverse scattering methods incorporate other optical techniques to improve resolution, speed, and functionality.

4. Three-dimensional inverse scattering

Live cells are highly dynamic in all three dimensions. Cell membrane fluctuation, mass transport, and motility are good indications of the organelle functionality and

viability, which are also linked to the health of the entire organ and body. To better study these processes, 3D mapping of the cell refractive index is very informative. Recently, this type of tomographic imaging has motivated researchers to solve 3D inverse scattering problems with visible light.

4.1. Early history

Since the early 1900s, the inverse scattering problem has been studied extensively in the X-ray spectrum with the goal of determining crystal structures [1]. In the optical regime, Wolf, proposed a theoretical model to solve the 3D inverse scattering problem, later known as optical diffraction tomography (ODT) [5]. ODT established a Fourier transform relation between the measured field and the object's susceptibility map. In the early years, due to the limitations of the computers and image sensors, experimental work exploiting this result was very limited. In the late 1950s, Oldendorf pioneered the use of X-ray sources for 3D tomographic reconstruction of macroscopic portions of the human body. Known as X-ray computed tomography (X-ray CT), the method allowed imaging of specific sections of the body without surgery [165]. In X-ray CT, the Radon transform technique describes the absorption line integral and is used to reconstruct the object in 3D [166].

X-ray diffraction exploits the field interaction with the *real part* of the dielectric permittivity, which generates *scattering* and informs about the *wavelength-scale* structure of an object. By contrast, *X-ray CT* exploits the field interaction with the *imaginary part* of the dielectric permittivity, which generates *absorption* and informs about the *absorption-length-scale* structure of an object. In 1985, Snyder et al. [167], following up on the work by Byer's group on optical absorption tomography [168], used laser interferometry to perform one of the earliest optical diffraction tomography experiments. They scanned the incident laser beam from 0° to 360° with a rotating mirror and measured in the far-zone ten projected interferograms, each spaced by 36°, with a 512 pixel by 512 pixel camera (50 μm square pixel size). Then, they extracted the phase and interpolated the data to 100 projections to reconstruct the 3D refractive index map of a glass rod using a computer. Their experiment demonstrated the feasibility of using optical diffraction tomography for 3D object reconstruction. In 1993, Schatzberg et al. proposed an iterative method, based on *a priori* object support model, to obtain the tomogram by measuring the scattered field intensity in the far-zone [169]. However, the iterative phase retrieval problem is ill-posed and only applies to certain types of objects, leaving the accuracy of the results in doubt, especially when measuring unknown objects. Due to all these difficulties, optical diffraction tomography did not make a big impact in its early years.

Thanks to the advances in computers and camera technologies, quantitative phase imaging has become a very active area. Driven by the imaging need in biomedicine and material science, many high sensitivity and high resolution QPI techniques have recently emerged and revived the research in optical diffraction tomography. Next, we first present the 3D inverse scattering theory and then review the recent works on optical diffraction tomography.

4.2. 3D inverse scattering theory

4.2.1. Direct problem

The 3D scattering problem can be described by the inhomogeneous Helmholtz equation, namely,

$$\nabla^2 U(\boldsymbol{r},\omega) + n^2(\boldsymbol{r})\,\beta_0^2(\omega)\,U(\boldsymbol{r},\omega) = 0, \qquad (4.1)$$

where $\beta_0(\omega) = \omega/c$ is the propagation constant, or wavenumber, in vacuum. $U(\mathbf{r},\omega)$ is the total field, which can be decomposed as $U(\mathbf{r},\omega) = U_i(\mathbf{r},\omega) + U_s(\mathbf{r},\omega)$, with $U_i(\mathbf{r},\omega)$ the incident field and $U_s(\mathbf{r},\omega)$ the scattered field from the object. The incident field satisfies the homogeneous wave equation, thus, reducing Eq. (4.1) to,

$$\begin{aligned}\nabla^2 U_s(\mathbf{r},\omega) + \beta^2(\omega)\,U_s(\mathbf{r},\omega) \\ = -\beta_o^2(\omega)\,\chi(\mathbf{r},\omega)\,U(\mathbf{r},\omega),\end{aligned} \qquad (4.2)$$

where $\beta(\omega) = \bar{n}\beta_0(\omega)$ is the average propagation constant in the medium, $\bar{n} = \langle n(\mathbf{r})\rangle$ is the spatially averaged refractive index, and $\chi(\mathbf{r},\omega) = n^2(\mathbf{r},\omega) - \bar{n}^2(\omega)$ is the susceptibility of the object. In the following, we will assume a dispersionless object, i.e., $\chi(\mathbf{r},\omega) = \chi(\mathbf{r})$. In order to directly solve for the scattered field, an assumption about the light-matter interaction is needed for simplification. For weakly scattering objects, the (first-order) Born and Rytov approximations are most commonly used. Both methods have been widely practiced in optical diffraction tomography. For the first-order Born approximation, the refractive index variation is assumed to be very small compared to the background, and the phase accumulation inside the object is assumed to be much smaller than 2π. Under this assumption, the scattered field originates only in single scattering events and is much smaller in amplitude than the incident field: $U_s(\mathbf{r},\omega) \ll U_i(\mathbf{r},\omega)$, resulting in a linear relation between the scattered field and the object susceptibility. On the other hand, the Rytov approximation assumes the total field as a phase function, $e^{\Psi(\mathbf{r})}$, where the function $\Psi(\mathbf{r})$ contains information about the scattered field [170]. Previous studies have shown that Rytov approximation is valid when the gradient of the refractive index is very small, making it more suitable for smooth and relatively large objects [see Chapter 8 of reference [171]]. Since we are interested in high-resolution imaging of thin samples, in the following formulation we use the first-order Born approximation to solve Eq. (4.2). Thus, the total field inside the object, $U(\mathbf{r},\omega)$, can be approximated by the incident plane wave, $U_i(\mathbf{r},\omega) = A(\omega)e^{i\beta(\omega)\hat{\mathbf{k}}_i\cdot\mathbf{r}}$, where $\hat{\mathbf{k}}_i = \hat{\mathbf{k}}_{\perp i} + \hat{\mathbf{k}}_{zi}$ is the propagation direction unit vector.

Equation (4.2) becomes,

$$\nabla^2 U_s(\mathbf{r},\omega)+\beta^2(\omega)U_s(\mathbf{r},\omega) = -\chi(\mathbf{r})\beta_0^2(\omega)A(\omega)e^{i\beta(\omega)\hat{\mathbf{k}}_i\cdot\mathbf{r}}. \quad (4.3)$$

Equation (4.3) can be solved in the wavevector space [29, 45, 172] by taking the 3D Fourier transform on both sides, namely

$$[\beta^2(\omega)-k^2]U_s(\mathbf{k},\omega) = -\beta_0^2(\omega)A(\omega)\chi[\mathbf{k}-\beta(\omega)\hat{\mathbf{k}}_i]. \quad (4.4)$$

Re-arranging and substituting the variables in Eq. (4.4), the scattered field $U_s(\mathbf{k},\omega)$ is solved as

$$\begin{aligned} &U_s(\mathbf{k},\omega)\\ &= -\beta_0^2(\omega)A(\omega)\chi[\mathbf{k}-\mathbf{k}_i]\frac{1}{2q}\left(\frac{1}{k_z-q}-\frac{1}{k_z+q}\right)\\ &= -\beta_0^2(\omega)A(\omega)\chi\left[\mathbf{k}_\perp-\beta(\omega)\hat{\mathbf{k}}_{\perp i},k_z-\beta(\omega)\hat{k}_{zi}\right]\\ &\quad\times\frac{1}{2q}\left(\frac{1}{k_z-q}-\frac{1}{k_z+q}\right), \end{aligned} \quad (4.5)$$

where q is defined as $q=\sqrt{\beta^2(\omega)-k_\perp^2}$ with $k_\perp=|\mathbf{k}_\perp|$. The two fractional terms in Eq. (4.5), $1/(k_z-q)$ and $1/(k_z+q)$, correspond to the forward scattered and backward scattered fields, respectively. By taking the inverse Fourier transform with respect to k_z, a new representation for the forward scattered field, U_f,and the backward scattered field, U_b, are obtained as a function of transverse wavevector, $\boldsymbol{k}_\perp$, axial distance, z, and angular frequency, ω

$$\begin{aligned} U_f(\boldsymbol{k}_\perp,z,\omega) &= -\frac{\beta_o^2(\omega)A(\omega)e^{iqz}}{2q}\\ &\quad\times\chi\left[\mathbf{k}_\perp-\beta(\omega)\hat{\mathbf{k}}_{\perp i},q-\beta(\omega)\hat{k}_{zi}\right], \end{aligned} \quad (4.6a)$$

$$\begin{aligned} U_b(k_\perp,z,\omega) &= \frac{\beta_o^2(\omega)A(\omega)e^{-iqz}}{2q}\\ &\quad\times\chi\left[\mathbf{k}_\perp-\beta(\omega)\hat{\mathbf{k}}_{\perp i},-q-\beta(\omega)\hat{k}_{zi}\right]. \end{aligned} \quad (4.6b)$$

Notice that, the scattered fields strongly depend on the optical frequency, despite the fact that the object is assumed dispersion-less. Importantly, Eqs. (4.6a) and (4.6b) relate the 3D Fourier transform of the object function to the 2D Fourier transform of the scattered field.

4.2.2. Inverse problem

Typically, the signal measured in interferometric microscopy is the cross-correlation between the scattered and the reference field. The cross-spectral density W, as a function of $\mathbf{k}_\perp$ and z, can be written as [172]

$$W(\boldsymbol{k}_\perp,z,\omega) = U_s(\boldsymbol{k}_\perp,z,\omega)U_r{}^*(z_R,\omega), \quad (4.6)$$

where $U_r(z_R,\omega)=A(\omega)e^{i\beta(\omega)\cdot z_R}$ is a plane wave propagating on along the optical axis z, and z_R is the propagation distance of the reference beam with respect to $z=0$ (defined by the scattering potential coordinate system). Thus, the general solutions to the inverse scattering are [45]

$$\begin{aligned} &\chi\left[\mathbf{k}_\perp-\beta(\omega)\hat{\mathbf{k}}_{\perp i},q-\beta(\omega)\hat{k}_{zi}\right]\\ &\quad=-2qW_f(\boldsymbol{k}_\perp,z,\beta)e^{-i(qz-\beta\cdot z_R)}\big/\left[\beta_o^2S(\beta)\right], \end{aligned} \quad (4.7a)$$

$$\begin{aligned} &\chi\left[\mathbf{k}_\perp-\beta(\omega)\hat{\mathbf{k}}_{\perp i},-q-\beta(\omega)\hat{k}_{zi}\right]\\ &\quad=2qW_b(\boldsymbol{k}_\perp,z,\beta)e^{i(qz+\beta\cdot z_R)}\big/\left[\beta_o^2S(\beta)\right], \end{aligned} \quad (4.7b)$$

where W_f and W_b are the forward and backward measured scattered, and $S(\beta)=|A(\beta)|^2$ is the incident field power spectrum. It should be noted that if the experiment measures $S(\lambda)$, a Jacobian transformation, i.e., $S(\beta)=-\lambda^2S(\lambda)/(2\pi\bar{n})$, is necessary to map $S(\lambda)$ to $S(\beta)$. Similarly, if $W_f(\lambda)$ and $W_b(\lambda)$are measured, as in Fourier-domain OCT, the Jacobian is necessary to describe these functions in the β domain.

Equations (4.7a) and (4.7b) are the foundation for 3D object reconstruction using optical diffraction tomography. From this equation, we see that one way to reconstruct the object in 3D is scanning the incident laser beam angle, given by $\hat{\mathbf{k}}_{\perp i}$ (or, equivalently, rotating the object around its axis) and measure the 2D cross-spectral density at each angle. Thus, the object 3D structure is determined through the Fourier transform relation. This laser angle-scanning method is the most commonly used in optical diffraction tomography. In section 4.3, we review some recent developments on this technique. The second way to perform the 3D reconstruction is scanning the optical frequency orβ and measuring the 2D cross-spectral function at each frequency, which is done in Fourier-domain optical-coherence tomography (OCT). The third way to perform 3D reconstruction is to scan the object through the focus. The method is presented in detail in Section 4.4. For the first two reconstruction methods, the transverse object reconstruction resolution is determined by the momentum transfer between the incident wavevector and the scattered wavevector, represented by the term $\mathbf{k}_\perp-\beta(\omega)\hat{\mathbf{k}}_{\perp i}$ in the object function. The depth resolution is determined by the spread in momentum transfer, which is $q-\beta\hat{k}_{zi}=\sqrt{\beta^2-k_\perp^2}-\beta\hat{k}_{zi}$ for transmission geometry and $-q-\beta\hat{k}_{zi}=-\sqrt{\beta^2-k_\perp^2}-\beta\hat{k}_{zi}$ for reflection geometry. Due to the longer axial projection, backscattering measurements have better sectioning effect than transmission measurements. The Ewald sphere representation can be used to visualize the 3D reconstruction under both geometries [45]. Due to the dependence of the

axial field distribution on the transverse wavevector, a sampling of the axial frequency k_z as $k_z = \sqrt{\beta^2 - k_\perp^2} - \beta\hat{k}_{zi}$ or $-\sqrt{\beta^2 - k_\perp^2} - \beta\hat{k}_{zi}$ is necessary prior to the 3D reconstruction. With the inverse scattering solutions provided by Eqs. (4.7a)) and (4.7b), one can use regularization or sparse deconvolution methods to obtain uniform object reconstruction [9, 14, 29, 173]. For transparent objects measurement, the transmission geometry is widely used. However, in confocal microscopy, the reflection geometry is usually pursued, allowing for better depth resolution. It is worth mentioning that the 3D reconstruction in Eq. (4.7b) can be also applied to the Fourier-domain OCT, without the far-field approximation typically used in interferometric synthetic aperture microscopy (ISAM) [14]. Lastly, Eqs. (4.7a) and (4.7b) simulate the scattering measurement in angle-resolved low-coherence interferometry (aLCI) for determining depth-resolved angular scattering from tissues [33, 146].

4.3. Laser diffraction tomography

Equations (4.7a) and (4.7b) establish the exact relationship between the scattered field and the object structure. For monochromatic waves, this equation recovers Wolf's optical diffraction tomography [5]. ODT combines X-ray diffraction principles with optical holography to obtain 3D tomographic imaging with visible light. Recently, several groups have demonstrated laser diffraction tomography, mainly with applications to label-free 3D imaging of biological samples. Here, we review several representative laser diffraction tomography works.

4.3.1. Angle scanning tomography

Angle-scanning laser diffraction tomography systems either scan the incident beam angle or rotate the object around its axis and record multiple phase images. The phase is retrieved usually by measuring with off-axis or phase-shifting interferometry techniques. Figure 6 shows a typical angle-scanning diffraction phase tomography system based on a Mach-Zehnder off-axis interferometer. An incident laser beam is split into a reference and signal field via a beam splitter. In the signal arm, a galvanometer mirror is used to scan the incident beam angle onto the specimen plane. The angle range is limited by the condenser numerical aperture. After the intermediate image plane, a 4f system is used to relay the image onto the detector, where the signal beam interferes with the reference beam to form an interferogram. The interferogram is recorded each angle and used to reconstruct the tomographic image using an inversion model.

In 2006, Charrière et al. demonstrated a tomographic imaging system using a diode laser based digital holographic microscope [10]. The experimental setup follows that of typical digital holographic microscopy (off-axis interferometry), which measures the interference between the reference beam and the sample beam in transmission geometry. Therefore, the measurement yields the complex scattered field at the CCD. At the sample plane, the object is embedded in a micropipette, which allowed the sample to rotate. The acquisition is done 90 times over 180° range with 2° steps at a rate of 1 Hz. By performing the Radon transformation and combining each of the 90 measurements, the tomography of a sample refractive index distribution is reconstructed. Figure 7, adapted from reference [10], shows the 3D refractive index reconstruction of a pollen cell using the digital holographic microscopy system. Figure 7a shows a central *xy* plane slice of the 3D refractive index mapping of the pollen cell, Fig. 7b shows slices along *yz* plane at different *x* positions, and Fig. 7c shows slices along *xz* plane at different *y* positions. The schematic of the slices are illustrated in Fig. 7d. From the tomographic measurements, the nucleus structure of the pollen cell can be clearly distinguished. Using the refractive index of the surrounding medium, 1.473, the refractive index of the nucleus is evaluated to be around 1.53. In addition, this 3D refractive index mapping can be potentially applied to determine the composition of the substances in the cell. The success of reconstructing the 3D refractive index proved that optical diffraction tomography is a feasible way to noninvasively visualize 3D cellular structure.

In the prior tomography system, fixing the object rotation axis could be problematic and the rotation tends to perturb the sample. A year later, Choi et al. presented another laser-based diffraction tomography method, referred to as tomographic phase microscopy (TPM) that utilizes a phase-shifting QPI method based on reference wave frequency-shifting using acoustic-optical modulators (AOMs) [8]. Unlike Charrière et al. this method scans the incident beam angle over a range of 60° using a galvanometer mirror in the illumination light path. Thus the sample is kept unperturbed, but the angular range covered is more limited than when rotating the sample. The method was applied successfully to imaging live cells and even multicellular organisms, such as a *Caenorhabditis elegans* (*C. elegans*). To use the 3D refractive index for examining the physiology changes in living cell, the authors investigated the effects of low concentration acetic acid on the morphology of the cell. These effects are well known to cause whitening of areas of the cervix, which is possibly due to the coagulation of the nucleus proteins, thus increasing the refractive index contrast between the nucleus and cytoplasm [174]. This method is widely used to identify the suspicious sites of precancerous lesions. Figures 8a and 8b are *xy* slices of the index tomogram of a HeLa cell cultured in normal medium and 3 minutes after culturing in medium containing 0.38% acetic acid, respectively. As expected, dramatic increases of the nucleus refractive index (from 1.36 to 1.39) and its inhomogeneity are observed. After replacing the acetic acid medium with normal medium for another 3 minutes, the cell nucleus refractive index distribution started to recover, but still remained somewhat higher than the baseline, as observed in Fig. 8c. To exemplify the multicellular organism tomographic imaging capability of TPM, a paralyzed *C. elegans* in nematode growth medium is imaged.

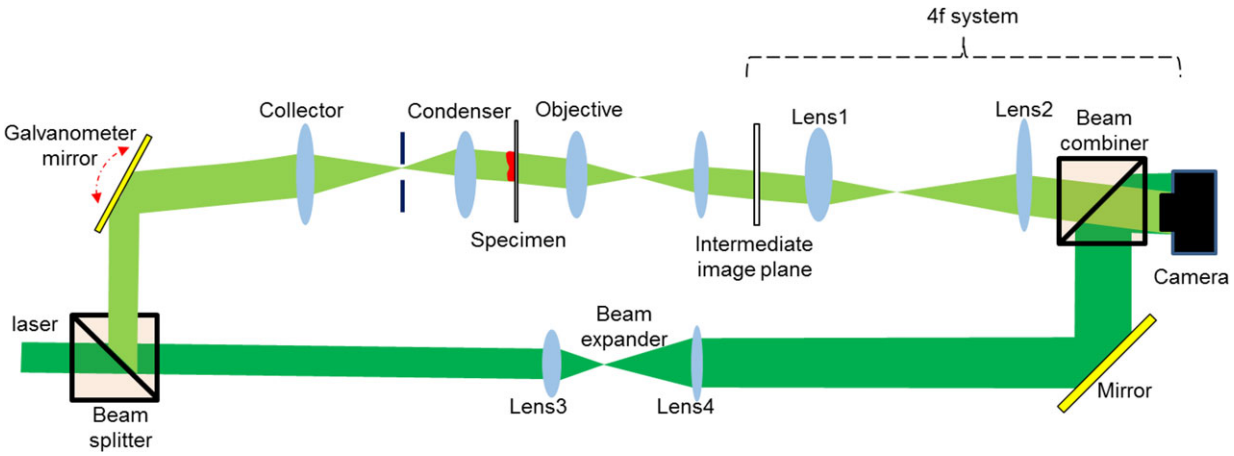

Figure 6 A typical angle-scanning diffraction phase tomography system based on a Mach-Zehnder off-axis interferometer.

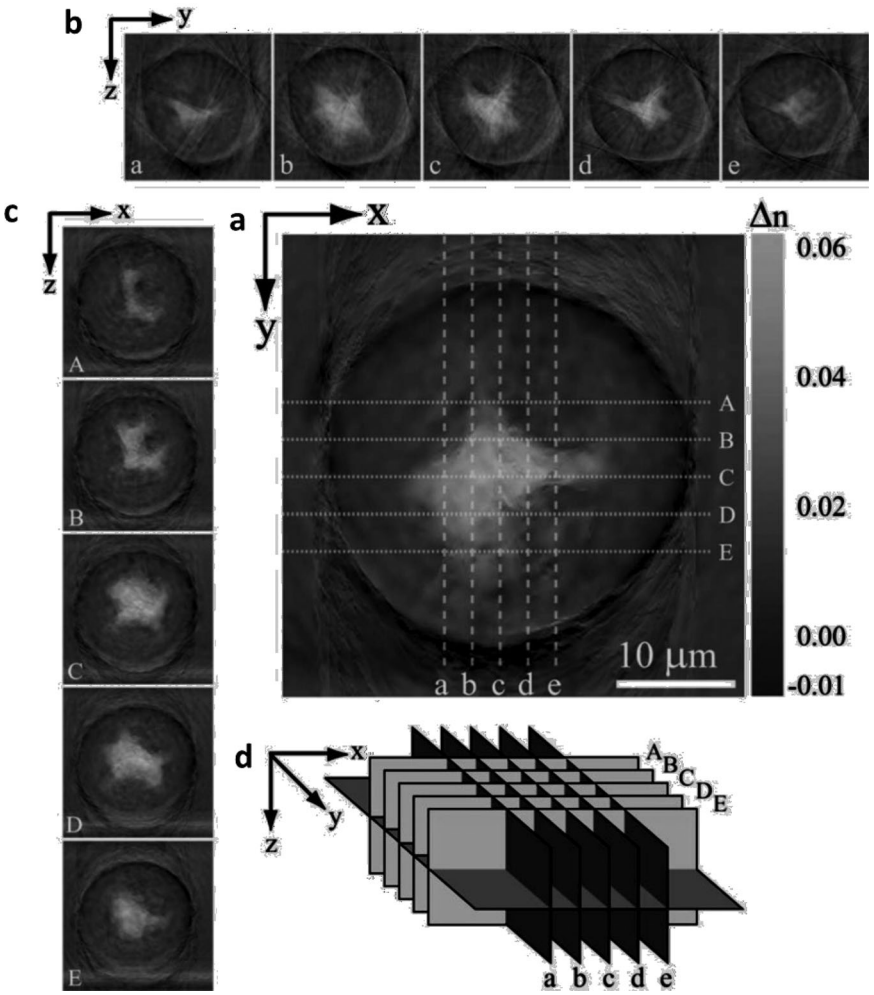

Figure 7 Tomography of a pollen cell RI: (a) cut along the *xy* plane in the middle of the pollen cell (b), cuts at different positions in the cell along the *yz* plane, and (c) the *xz* plane, and (d) schematic of the presented cuts. The figures are adapted from reference [10] with permission.

Figure 8d shows a mosaic *xy* slice of the index tomogram of the whole *C. elegens*, where the pharynx and digestive tract are clearly revealed.

Choi et al. and Charrière et al. both used the filtered back-projection reconstruction method based on the Radon transform, like in X-ray CT, and treated the phase as a line integral of the refractive index along the projection direction and ignored the diffraction effect. Therefore, the filtered back-projection reconstruction method hindered them in achieving high transverse resolution, as this method is only suitable for samples thinner than the depth of field. In 2009, Sung et al. proposed using a Rytov approximation

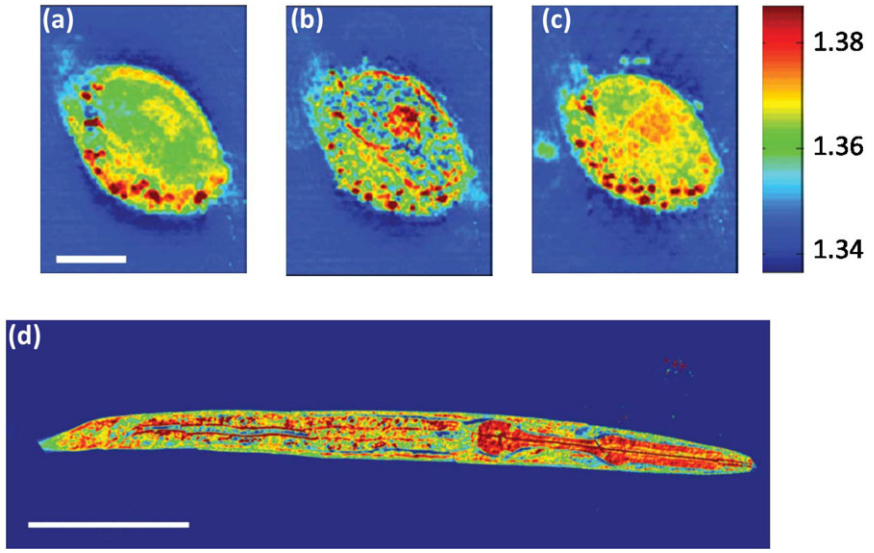

Figure 8 Effects of acetic acid on HeLa cell morphology and imaging of a *C. elegans* multicellular organism. (a) An x-y slice of the index tomogram from a HeLa cell in normal culture medium. (b) The x-y slice of the index tomogram from the HeLa cell after 3 minutes in medium containing 0.38% acetic acid. (c) 3 minutes after replacing the acetic acid with the normal medium. (d) A mosaic x-y slice of the index tomograms of the *C. elegans*. The scale bar for (a)-(c) is 10 μm and 50 μm for (d). Color bar represents the refractive index. The figures are adapted from reference [8] with permission.

based optical diffraction tomography model to improve the 3D reconstruction performance and the transverse imaging resolution, 0.35 μm, compared to that of Choi's earlier system, 0.5 μm [43]. However, due to the limited angle coverage of the scanning beam in TPM, certain sample frequency information is missed and this resulted in reconstruction artifacts such as sample elongation along the optical axis. To overcome this issue, a regularization method, based on sample refractive index positivity and piece-wise smoothness constraints, has been applied to the TPM numerical reconstruction model [9].

More recently, Kim et al. [175] provided an application of angle scanning optical diffraction tomography to image red blood cells parasitized by Plasmodium falciparum (Pf-RBCs) and compared the refractive index distribution of these cells with normal RBCs. In this work, reconstructions from the diffraction tomography method are compared with those from the projection method, which assumes no diffraction from the sample. The result, shown in Fig. 9, reveals that the diffraction tomography method reconstructs the refractive index distribution more accurately than the projection method because it recovers the scattering map by taking into account the diffraction through the sample.

4.3.2. Synthetic aperture tomography

In the previous angle-scanning laser ODT system, due to the laser speckle phenomena and the limited coverage of the scanning angle, these systems usually do not have good sensitivity and the resolution is limited to $\lambda/2$ or worse. In 2013, Cotte et al. proposed a synthetic aperture digital holographic microscopy approach by using two identical 63x/NA = 1.4 oil immersion objectives, and scanning the aperture of the upright objective [12]; see the system schematic in Fig. 10a. Due to the use of high NA objective lenses, their system can collect the scattered light with an angle coverage close to 2π; thus, they call their technique quasi-2π-digital holographic microscopy (2π-DHM). Figure 10b shows a synthesized 2π (k_x, k_y) plane measurement, expanding the original frequency space signal coverage by a factor of two. Figure 10c shows the (k_z, k_x) plane signal which is due to the low-pass filtering of system coherent transfer function, and Fig. 10d is the complex deconvolved signal in Fig. 10c. The 3D reconstruction uses the complex deconvolution algorithm and achieves transverse imaging resolution more than a factor of two better than the diffraction limit (experimentally claimed 90 nm transverse resolution). This system has been successfully applied to imaging of neural network, porous cell frustule (diatom), and *E. coli* in 3D.

4.3.3. New developments

In ODT, the object reconstruction resolution is determined by the coverage in the momentum transfer, $\mathbf{p} = \mathbf{k}_s - \mathbf{k}_i$. In 2012, Sentenac et al. proposed a grating-assisted optical diffraction tomography system to achieve $\lambda/10$ resolution [30]. By putting the sample on a nanostructured metallic films and scanning the illumination angle, one can generate surface plasmon modes that have very high spatial frequencies and can couple them into the far field, thus, tremendously increasing the object reconstruction resolution. In their simulation, they resolved two dipole like glass objects separated by $\lambda/10$ by using an inverse model based on Green tensors. For weakly scattering objects, the first-order Born approximation or the Rytov approximation are usually good approximations to the field inside the object. However, for non-weakly scattering objects, the field inside the object is complicated and these approximations are invalid, which prohibited accurate reconstruction of the object. To overcome this issue, the same group developed an iterative method to solve the exact field inside the object and to correctly reconstruct the object structure [176, 177], which experimentally enabled them to realize transverse superresolution in optical diffraction tomography. The iterative Green tensor approach by Sentenac et al. is computationally expensive.

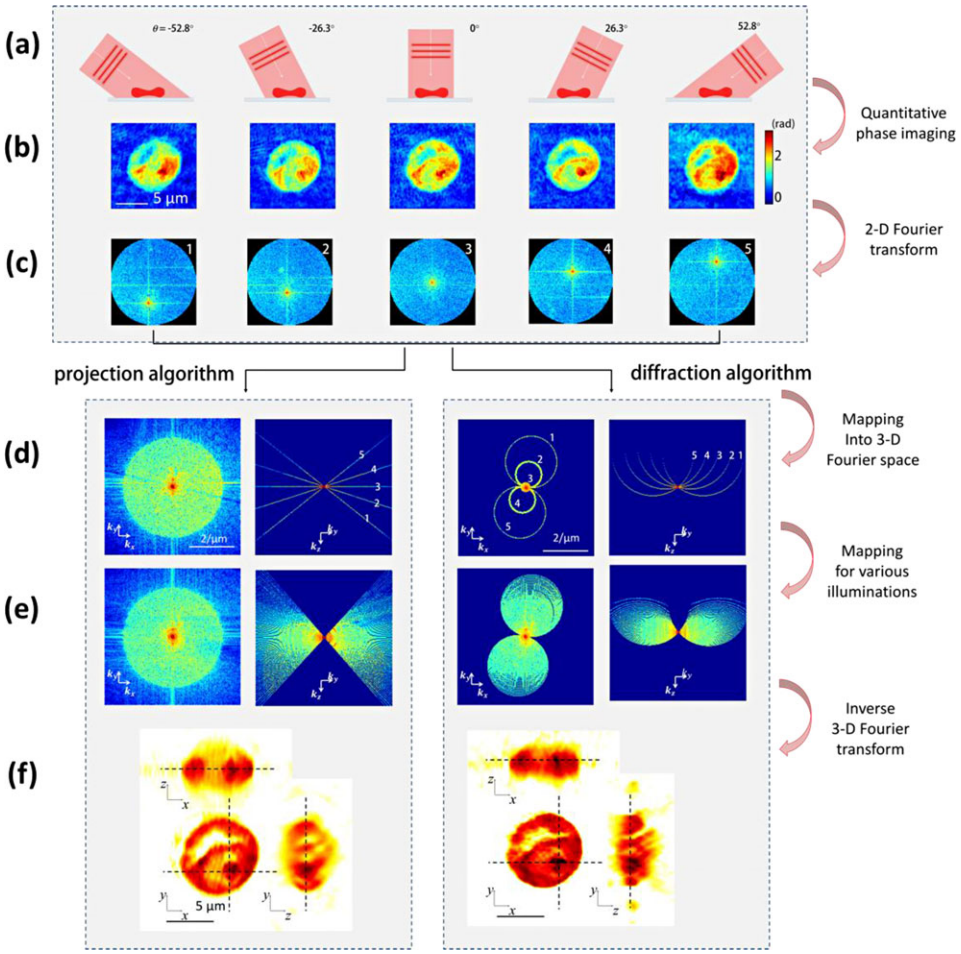

Figure 9 Comparison of various 3D reconstruction algorithms. (a) A schematic diagram of various angles of illuminations on a sample. (b) Quantitative phase images of a Plasmodium falciparum-red blood cell (Pf-RBC) in the trophozoite stage measured at various illumination angles and (c) corresponding spectrum in Fourier space. (d) and (e) show a side by side comparison of the Fourier space object functions reconstruction using the projection algorithm (left panel) and the diffraction algorithm (right panel), respectively; (d) shows the amplitude distributions of the object functions reconstructed by both algorithms with five representative illuminations angles and (e) shows the reconstruction with the full illumination angles. (f) Reconstructed RI maps of the Pf-RBC at the trophozoite stage.

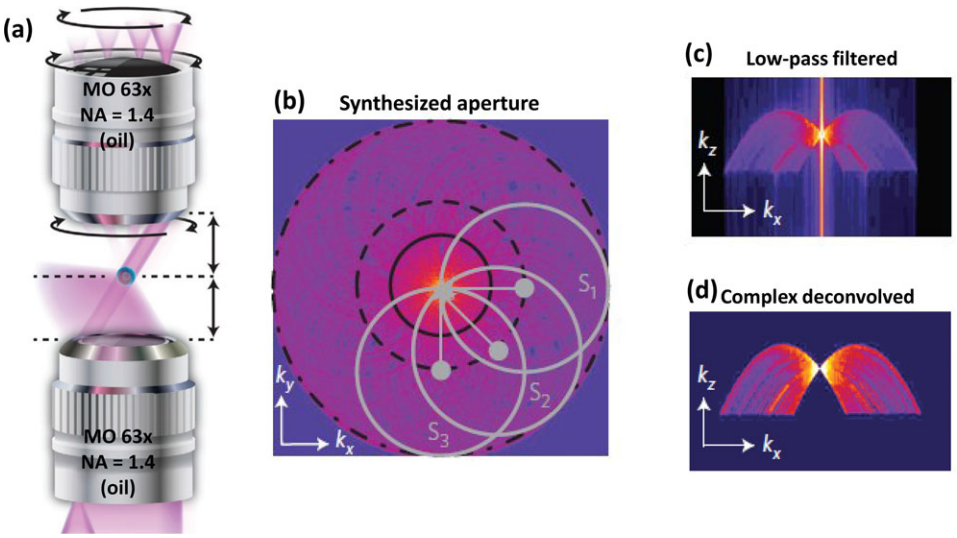

Figure 10 A description of the synthetic aperture homographic microscopy. (a) A system schematic description. (b) The measured and synthesized aperture. (c) The low-pass filtered (k_z, k_x) plane spatial frequency signal due to the system coherent transfer function. (d) The complex deconvolution of the signal in (c). The figures are adapted from reference [12] with permission.

Very recently, Psaltis' group at EPFL applied machine learning to diffraction tomography [178]. In this paper, the authors trained an artificial neural network to reproduce a complex field which is measured from an angle-scanning phase tomographic system. The network is constructed by the beam propagation method and dividing the sample into thin slices in the propagation direction. The beam propagation method models the scattering process, while an error backpropagation method is used to train it. With the trained network, a 3D refractive index map of the object, which matches the experimental observations, is recovered. Figure 11 shows an example of a live cell 3D imaged using this

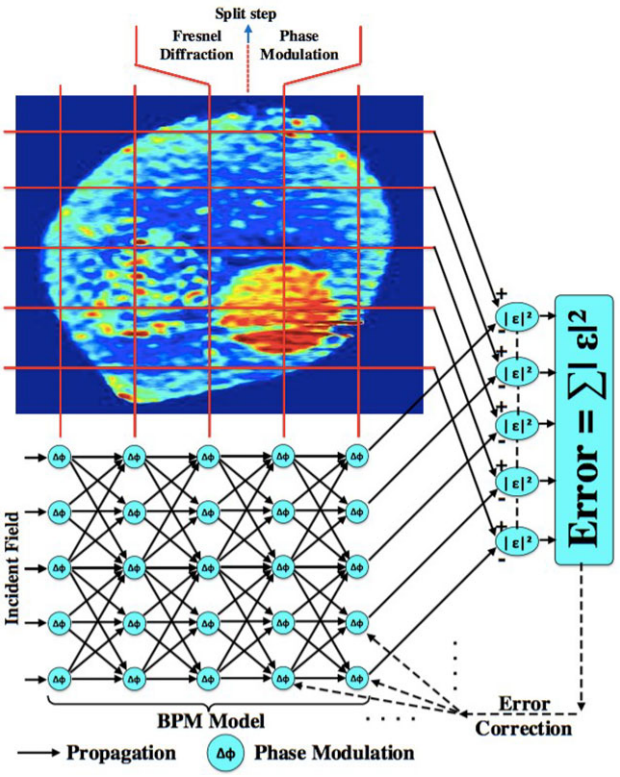

Figure 11 An artificial neural network is configured to simulate the propagation of light through an inhomogeneous medium (a cell). The difference between the predictions of the network and the experimental measurements is minimized by modifying the parameters of the neural network. The parameters of the trained network are directly related to the index distribution of the cell.

learning method. By modifying the parameters of the neural network, the difference between the network prediction and the experimental measurements is minimized, leading to a more precise recovery of the 3D index distribution of the cell.

In nature, many biological specimens possess anisotropic properties. Polarization microscopy, or pol-Scope developed by Oldenbourg et al. in mid-1990s [179], is capable of providing high image contrast, due to birefringence, without sample staining. Pol-Scope, particularly sensitive to the fibrous cell structures, was made possible to observe in real-time mitotic spindle isolating from fertilized sea urchin egg, newt lung epithelial cell in mitosis, etc. In 2008, Wang et al. demonstrated a polarization-resolved quantitative phase microscopy to image transparent and anisotropic samples [180]. Nevertheless, in literature, there have been very few publications on polarization-resolved optical diffraction tomography. In Wolf's initial ODT theory, only the scalar field inverse scattering solution is provided. In this paper, he promised to publish a vector field formulation, but it was not done until 33 years later by Lauer [181]. Using the vector-field diffraction tomography theory, Zhang et al. demonstrated a full-polarized diffraction phase tomography system [182]. With the polarization-resolved tomography system and an inversion model based on vector-field ODT, the authors reconstructed the permittivity map of nano-rod structures of 100 nm wide, 300 nm long, and 140 nm high with a resolution of about 170 nm.

Most of the optical diffraction tomography systems are based on interferometric measurements, but the complex field can be also retrieved with only intensity measurements, under some strong assumptions [128, 183, 184]. In 2013, G. Zheng et al. proposed Fourier ptychographic microscopy [185], an imaging technique similar to synthetic aperture imaging, which measures intensity at different illumination angle and extends the fields of view by using a low-numerical aperture objective lens. Fourier ptychographic microscopy has been used for 2D phase imaging of large stained samples to producing high resolution gigapixel images, but recently it has been demonstrated for unstained biological imaging in 3D [186]. Sharing the similarity of synthetic aperture imaging, Fourier ptychographic microscopy also holds promises for optical diffraction tomography. In particular, it can be combined with coded aperture to perform compressive sensing, reduce the number of measurements, and increase the imaging photon flux, thus increasing the speed for tomographic reconstructions [187, 188]. 3D imaging using Fourier ptychographic or the conventional interferometric ODT systems typically involves illumination angle scanning. Very recently, P. Hosseini et al. developed a fast ODT system that scans the color of three illumination beams coming from a supercontinuum source by using an acousto-optic tunable filter [189].

4.4. *White-light diffraction tomography*

Most of the previous optical diffraction works are based on non-common-path laser interferometric QPI; thus, the imaging suffers from laser speckle and mechanical noise. To reconstruct the depth dimension, laser angle scanning, objection rotation, and aperture synthesis approaches were proposed. White light is temporally incoherent, thus, immune to speckle noise, offering very high sensitivity phase measurement. In 2014, Kim et al. provided an inverse scattering solution for spatially coherent, temporally incoherent light by solving the wave equation in the wavevector space under the first-order Born approximation. This method is referred to as *white-light diffraction tomography* (WDT). WDT is an extension of Wolf's optical diffraction tomography (ODT) to broadband illumination. Also, WDT operates in imaging rather than a scattering geometry, offering higher sensitivity than traditional far-field measurements. WDT measures the complex scattered field using a common-path phase-shifting QPI technique called SLIM, and solves the inverse scattering problem to recover the structure of a scattering medium with sub-micron resolution in all three dimensions. In the following sections, we describe WDT in more detail.

4.4.1. White-light diffraction tomography theory

Unlike other previous approaches by Wolf or interferometric synthetic aperture microscopy (ISAM) [14], WDT

employs a new method to solve the inverse scattering problem. Specifically, the calculation is performed in the wavevector space instead of the traditional, spatial domain calculations using the Green function. Here, we use the results from section 4.2 to formulate WDT. In QPI, the interference between the scattered field and the plane wave reference is measured. Therefore, the cross-spectral density, $W_{12}(\mathbf{k}_\perp, z; \omega)$, is the measured quantity. For transmission QPI system, this quantity can be expressed as,

$$W_{12}(\mathbf{k}_\perp, z; \omega) = -\frac{\beta_0^2(\omega) S(\omega)}{2q} e^{i[q-\beta(\omega)]z} \times \chi(\mathbf{k}_\perp, q-\beta(\omega); \omega), \quad (4.8)$$

where $S(\omega) = |A(\omega)|^2$ is the power spectrum of the incident field. In SLIM, a broadband source is used. Therefore, according to the central ordinate theorem of Fourier transformation, the temporal cross correlation at zero-delay can be evaluated by integrating Eq. (4.8) over the frequency,

$$\Gamma_{12}(k_\perp, z; 0) = -\int_0^\infty \frac{\beta_0^2(\omega) S(\omega) e^{i(q-\beta(\omega))z}}{2q} \times \chi(k_\perp, q-\beta(\omega); \omega) d\omega. \quad (4.9)$$

In order to evaluate the integral, the frequency variable, ω, in Eq. (4.9) can be replaced by an integral over β using the relation $\beta = \bar{n}\omega/c$, thus,

$$\Gamma_{12}(k_\perp, z; 0) = -\frac{c}{2\bar{n}^3} \int_0^\infty \frac{\beta_0^2 S(\beta c/\bar{n}) e^{i(q-\beta)z}}{q} \times \chi(k_\perp, q-\beta) d\beta. \quad (4.10)$$

By defining a new variable, $Q = q - \beta = \sqrt{\beta^2 - k_\perp^2} - \beta$, as a re-sampling of k_z, Eq. (4.10) can be simplified further by replacing β and q with $\beta = -(Q^2 + k_\perp^2)/2Q$ and $q = (-Q/2 + k_\perp^2/2Q)$, respectively. With the Jacobian transformation, $d\beta = (-1/2 + k_\perp^2/2Q^2) dQ$ and $S(\beta c/\bar{n}) \leftrightarrow (\bar{n}\lambda^2/2\pi c) S(\lambda)$, which is necessary since the measurement of spectrum is typically done as a function of wavelength, Eq. (4.10) becomes,

$$\begin{aligned}\Gamma_{12}(k_\perp, z; 0) &= \frac{1}{8\bar{n}^2} \int_0^\infty \frac{\left(Q^2 + k_\perp^2\right)^2}{Q^3} S \times \left(-\frac{Q^2 + k_\perp^2}{2Q}\right) \chi(k_\perp, Q) e^{iQz} dQ \\ &= \frac{1}{8\bar{n}^2} FT_Q^{-1} \times \left[\frac{\left(Q^2 + k_\perp^2\right)^2}{Q^3} S\left(-\frac{Q^2 + k_\perp^2}{2Q}\right)\right] \textcircled{v}_z \chi(k_\perp, -z) \\ &= \Sigma(k_\perp, -z) \textcircled{v}_z \chi(k_\perp, -z) \quad (4.11a)\end{aligned}$$

Alternatively, in the 3D spatial frequency space, $(k_\perp, Q)$, the cross correlation becomes,

$$\Gamma_{12}(k_\perp, Q) = \Sigma(k_\perp, Q) \chi(k_\perp, Q). \quad (4.11b)$$

Equation 4.11 relates *the coherent transfer function* (CTF), Σ, the object function, χ, and the measurement Γ_{12}. CTF describes the instrument response from the imaging system, including the incident spectrum and also the numerical aperture, which limits the $k_\perp$ range of the system. Therefore, the sectioning effect of the imaging system is determined by the temporal coherence function and the numerical aperture. Equation (4.11a) shows that the depth information of the scattering potential, $\chi(k_\perp, z)$, can be recovered by measuring at different z-positions. Therefore, by scanning the focus through the sample in the imaging system followed by a deconvolution in the spatial domain, the object's 3D distribution can be obtained.

4.4.2. Point-spread function calculation

In order to visualize the system response, the point spread function (PSF) of the system is numerically calculated by taking the 3D inverse Fourier transform of the CTF. Using the measured incident spectrum and numerical aperture of the imaging system, the complex CTF is numerically calculated for the 63x/1.4NA objective. Through the inverse Fourier transform, the complex PSF is calculated and then the argument of the complex PSF is taken, since the imaging system maps the phase shift through the object. Figure 12a shows the CTF, or the frequency coverage of the imaging system. In this plot, it is apparent that the coverage of axial spatial frequency, k_z, is larger at larger transverse spatial frequency components, $k_\perp$. This result correctly shows that, for larger transverse spatial frequencies of the scattered light, the optical sectioning effect is stronger. A comparison between the calculated PSF and measured PSF, obtained by measuring a microbead, is shown in Fig. 12b. The numerically calculated PSF gives a transverse resolution of 350 nm and an axial resolution of 890 nm, while the measurement shows that the actual resolution of the system is 398 nm in the transverse dimension and 1218 nm in the axial dimension.

Further numerical calculations of the PSF in the x-z (transverse and longitudinal) domain for various values of NA, ranging from 0.1 to 2, are shown in Fig. 13a. As expected, at higher NAs, not only is the resolution better, but there is also stronger optical sectioning. Figures 13b and 13c show plots of the transverse and longitudinal resolution, evaluated at the full width half maximum (FWHM), of each calculated PSF as a function of inverse NA and inverse NA squared, respectively.

4.4.3. Experiments

In order to get the 3D distribution of the complex scattered field, a SLIM system [44] has been used. SLIM, as

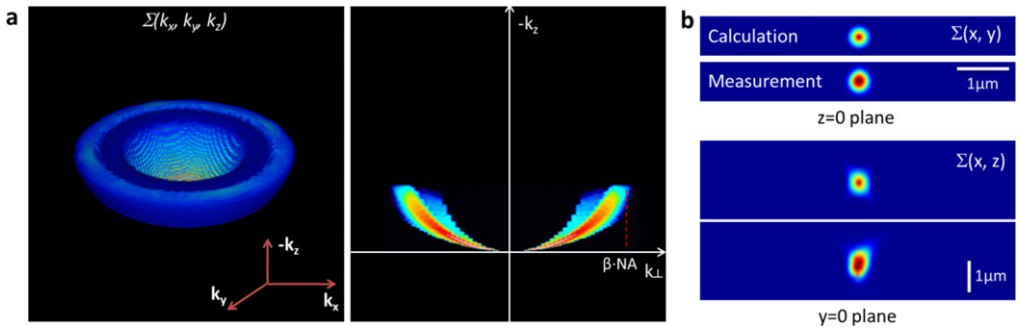

Figure 12 Coherence transfer function and resolution of a SLIM system using 63x/1.4NA objective. (a) Calculated coherent transfer function shown in the wavevector domain. The transverse spatial frequency is cutoff by the numerical aperture (1.4) of the objective. (b) A comparison between the calculated point spread function and the measure point spread function. (top) The transverse cross-section of the PSF and (bottom) the axial cross-section of the PSF. The figures are adapted from reference [29] with permission.

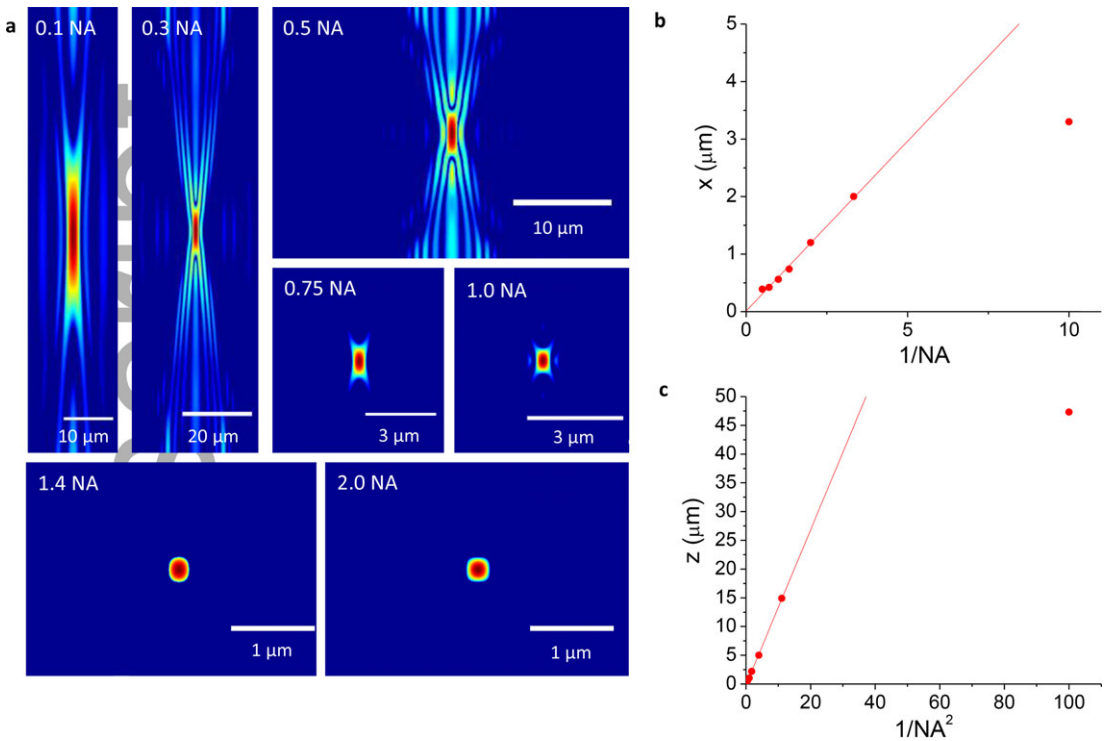

Figure 13 PSF calculated for various values of NA. (a) The axial cross section of the PSF. (b) FWHM of the calculated PSFs in the transverse direction as a function of inverse NA. (c) FWHM of the calculated PSFs in the longitudinal direction as a function of inverse NA squared. The figures are adapted from reference [29] with permission.

described in Fig. 1, is based on a conventional phase contrast microscope, implemented with an external module that adds four different phase shifts (0, $\pi/2$, π, $3\pi/2$) to the unscattered field and retrieves the quantitative phase through the sample by combining these four frames. As shown in Eq. (4.11b), the measurement through SLIM can be considered as a convolution between the PSF of the optical system and the structure of the object. Therefore, a deconvolution process on the acquired data is performed to reconstruct the 3D structure of the object. Quantitative phase images from SLIM, with very low noise level, are converted to a sparse representation. Based on this property, WDT implements a sparse deconvolution algorithm for 3D reconstruction. In order to assess the performance of deconvolution, the measured PSF (63 $\times$ /1.4NA) is deconvolved by the calculated PSF. The FWHM of the PSF after the deconvolution process was 285 nm in the transverse dimension and 967 nm in the axial dimension, which is equivalent to 1.3x decrease in FWHM. This proves that WDT successfully models the imaging system and increases the resolution by the deconvolution process suggested by the theoretical explanation. In the following section, the 3D reconstruction results from WDT is presented.

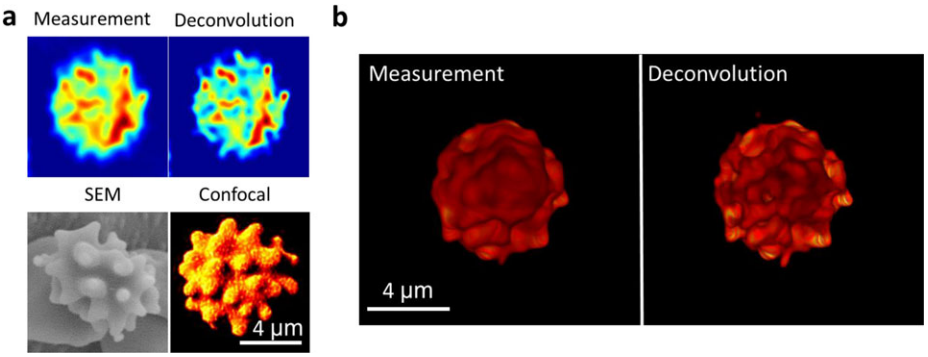

Figure 14 Spiculated red blood cell images of WDT. (a) Comparison of the SLIM measurement and WDT processed image along with an SEM image and a confocal image of a similar cell. (b) 3D rendering of SLIM and WDT images of the RBC. The figures are adapted from reference [29] with permission.

4.4.4. Results

To demonstrate the capability of WDT in imaging transparent 3D objects, the authors illustrated results mainly involving unlabeled live cells. First images, taken with WDT, show spiculated red blood cells (RBC), also known as echinocytes. In order to reconstruct the 3D structure of these cells, first, quantitative phase images at different z-position were obtained using SLIM with 40 × /0.75NA objective, and then the deconvolution process was applied to obtain WDT images. In this case, a new PSF calculated for the 40x objective was used. One image from each of these two stacks, SLIM measurement and WDT reconstruction, is shown in Fig. 14a, along with an image taken under scanning electron microscope (SEM) and confocal fluorescence microscope. Finer structures are revealed clearly in the WDT image compared to SLIM measurement. Using these two stacks, the 3D structure of the cell was rendered as shown in Fig. 14b. The protrusions in the cell membrane are much more pronounced in the WDT reconstruction, compared to the SLIM reconstruction case, where it is undistinguishable between different spicule structures.

Another sample of interest is *Escherichia coli* (*E. coli*) cells. Recent studies using high-resolution fluorescence microscopy have shown that there are subcellular localizations of proteins in a helical structure [190–192]. Unlike previous studies, WDT images an E. coli cell at high resolution with no fluorescence labeling. Figures 15a and 15b show the original measurement and the WDT processed image, respectively. Helical subcellular structure is clearly resolved in the WDT image as shown in the reconstruction in Fig. 15f. In Figs. 15c, 13d and 15e, different cross-sections, indicated in Fig. 15a and 15b, are presented to show the resolved helical structure in all three directions.

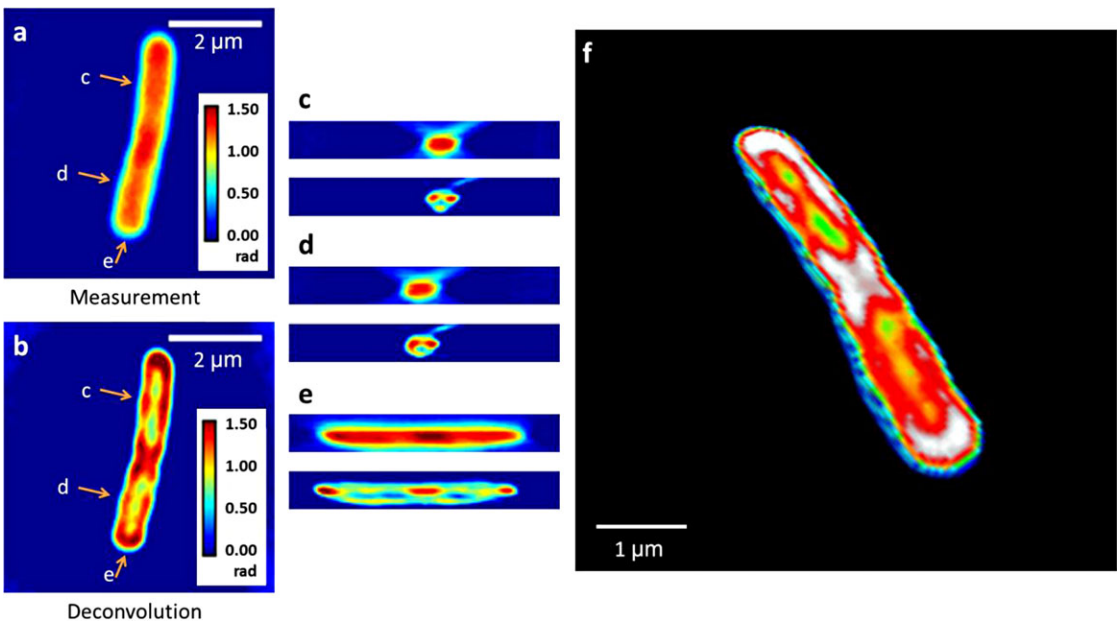

Figure 15 WDT of an E.coli. (a) SLIM measurement of an E.coli. (b) WDT image of the same E.coli, shown at the same frame as (a). (c-e) cross-section of the SLIM and WDT images taken at the locations indicated in (a) and (b). (f) 3D rendering of the WDT image showing only the bottom half of the cell in order to emphasize the helical sub-cellular structure. The figures are adapted from reference [29] with permission.

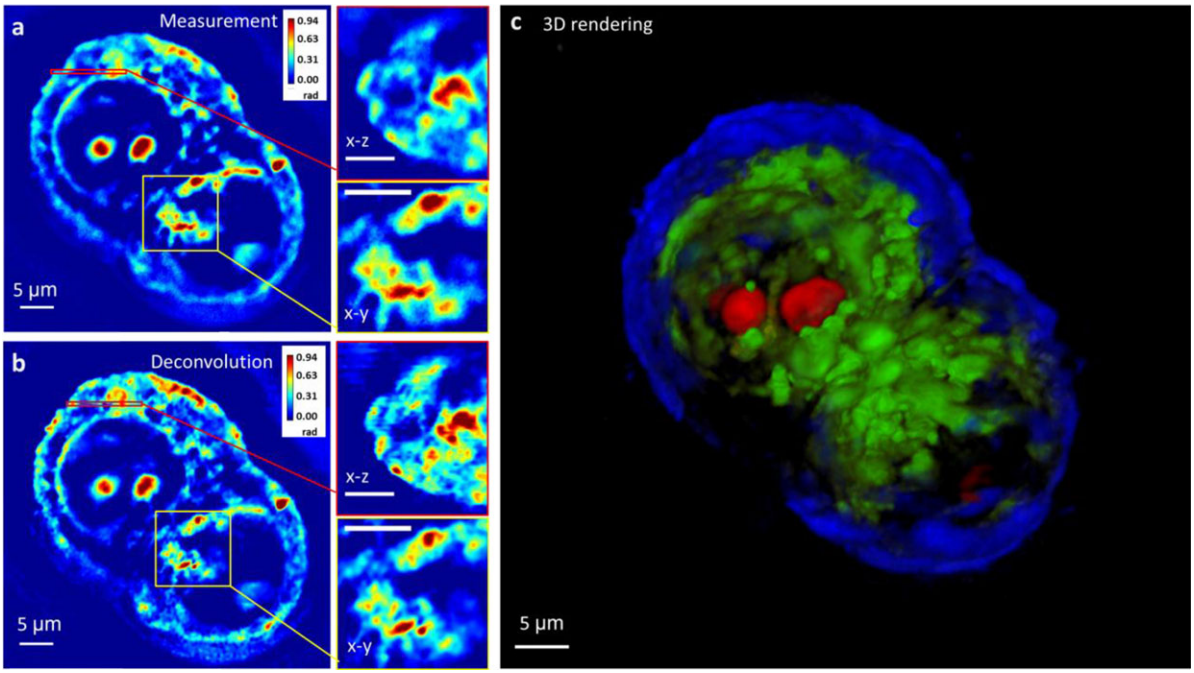

Figure 16 WDT of an HT-29 cell. (a) SLIM measurement of the cell, a zoomed-in cross section (top right) and a zoomed-in area (bottom right). (b) WDT image of the same field of view as (a). (c) 3D rendering of the WDT image, false-colored based on the phase value and morphology, showing different parts of the cell (red: nucleoli, green: nuclear membrane, blue: cell membrane). All scale bars represent 5 μm. The figures are adapted from reference [29] with permission.

WDT can also be used to image eukaryotic cells. 3D reconstruction of a human colon adenocarcinoma cell (HT-29) was demonstrated by WDT using a 63 $\times$ /1.4NA objective. The cell is imaged right after mitosis, and Fig. 16a and 16b show one z-slice of the SLIM measurement and the WDT image. On the bottom of each image, magnified transverse and axial cross-sections are shown for better visualization the resolution enhancement by WDT. In the WDT image, as expected, a sharper image is observed. Figure 16c shows a false-colored 3D rendering of the WDT stack to show different parts of the cell in 3D. Each portion of the cell was selected first by thresholding based on the phase values, and then refined based on the morphology. This is a clear demonstration of the capability of WDT in 3D imaging, granted by the quantitative phase imaging capability.

WDT can also be extended to 4D imaging, i.e., time-resolved tomography. Since the imaging system uses a commercial phase contrast microscope, it has all the peripherals such as environmental control and cell incubating chamber. In addition to these accessories, the high-precision microscope stage ensures the imaging to be performed at specific positions in space without drifting or shifting over time. With these capabilities, the technique has imaged HeLa cells in 3D over a 24 hour period. Figure 17 shows a HeLa cell at three different z-positions, taken from full 3D images obtained at each hour. Dynamics of the cell membrane and also division of the cell nucleoli indicated that the cell remained viable throughout imaging.

4.4.5. Discussion

WDT, which uses spatially coherent and temporally incoherent light, has been used to retrieve 3D structures of unlabeled cells. The depth information is obtained by simply scanning the focus through the object along the optical axis. The reconstruction algorithm requires a physical understanding of light-matter interaction between broadband light and a weakly scattering object. WDT theory, which generalizes Wolf's diffraction tomography, describes this interaction in the imaging system. WDT is a common-path, label-free imaging system, which uses visible light, and is highly stable for 3D imaging over days. Recently, we have improved the hardware and software in our WDT system to allow for faster acquisition of 3D dynamics. We envision that WDT will become a standard 3D imaging modality in cell biology in the future.

WDT has many advantages over other optical tomography methods, but also has limitations. For example, due to the use of the first-order Born approximation and white-light source, WDT is limited to transparent (negligible absorption) and dispersionless (refractive index is independent of wavelength) samples.

5. Summary and outlook

In summary, we have discussed a number of 2D and 3D inverse scattering methods based on quantitative phase imaging. By measuring the complex scattered field in QPI and

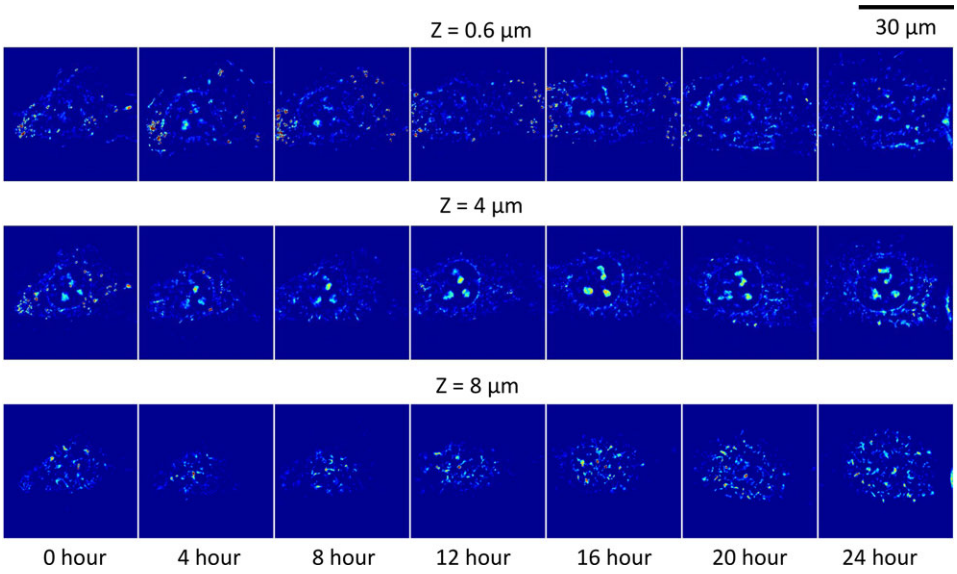

Figure 17 WDT image of a HeLa cell imaged over 24 hours. Images at three depth positions are shown to emphasize the bottom of the cell, middle of the cell, and the top membrane of the cell. The figures are adapted from reference [29] with permission.

solving the inverse scattering problem, reconstruction of transparent structures becomes possible. In this review, the relationship between light scattering and QPI has been first established and demonstrated by 2D inverse scattering methods. Recent advances in imaging speed and resolution, along with mechanical motion control in QPI, have directly benefited the research in solving inverse scattering problems. As a result, new breakthroughs in high resolution tomographic imaging of transparent objects have been achieved. Optical diffraction tomography, initially proposed by Wolf, solved the inverse scattering problem for coherent light sources. Recently, the theory has been extended to temporally broadband light sources by Interferometric Synthetic Aperture Microscopy and White-light Diffraction Tomography. These theoretical developments have been successfully demonstrated in experiments, enabling high-resolution label-free 3D imaging. All of these inverse scattering methods have been growing rapidly in their applications towards various fields of studies, ranging from biomedical studies to material metrology.

With the remarkable findings and advances in the past two decades, quantitative phase imaging has already shown its capability in studying biological samples. Its applications range from basic biological studies such as cell growth and cell dynamics to clinical applications such as blood screening and tissue diagnosis. We envision that the need to visualize 3D structures noninvasively using these powerful methods will grow rapidly in the coming years. It has become increasingly clear that studying cells and microenvironment in three dimensions more accurately depicts live tissue conditions. For example, studying cell nucleus, the largest organelle in the cell, is important for understanding the whole cell functionality, especially the cell viability. Using the 3D quantitative imaging techniques, certain physiological quantities such as cell nucleus shape, size, and dry mass can be determined. Recently, these parameters have been used as biophysical markers for stem cell identification and carcinogenesis studies [193, 194]. In conclusion, the rapid expansion of the field and the applications of quantitative phase imaging and inverse scattering methods indicate that the field is now approaching the critical mass of being used broadly by biologists everywhere.

Acknowledgments. This work was supported by NSF grants: CBET-1040461 MRI (to GP and LLG), CBET-0939511 EBICS (to GP), and by the Beckman Foundation Graduate Fellowship (to RZ and TK).

Received: 17 December 2014, **Revised:** 17 November 2015, **Accepted:** 18 November 2015

Published online: 18 December 2015

Key words: quantitative phase imaging, light scattering, Microscopy, interferometry, phase retrieval, live cells, tissues, label-free.

Dr. Taewoo Kim is an Optical Engineer at Phi Optics, Inc. He received the Ph.D. in Electrical Engineering in 2015 from the University of Illinois at Urbana-Champaign, where he also received his B.S. and M.S. degrees. He authored 19 journal publications, 25 conference presentations and 2 patents. He received Beckman Institute Graduate Fellowship, SPIE Optics & Photonics Education Scholarship and IEEE Photonics Society Graduate Student Fellowship in 2014.

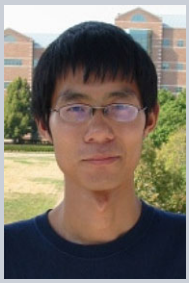

Since 2014, **Dr. Renjie Zhou** has been a postdoctoral researcher in G. R. Harrison Spectroscopy Lab at MIT. His current research focuses on biomedical imaging. Dr. Zhou received a PhD degree in Electrical Engineering from the University of Illinois at Urbana-Champaign. He also obtained MS degrees from the University of Arizona and the University of Dayton, and a BS degree from Huazhong University of Science and Technology in 2008.

Dr. Lynford Goddard is an Associate Professor of Electrical and Computer Engineering at the University of Illinois. His group fabricates, tests, and models photonic sensors, circuits, and instrumentation, develops novel device processing techniques, and applies quantitative phase microscopy for semiconductor wafer metrology. Dr. Goddard received the AAAS Early Career Public Engagement Award in 2011 and the PECASE award in 2010. He is co-author of over 160 publications and 6 patents.

Dr. Gabriel Popescu is Associate Professor in Electrical and Computer Engineering, UIUC. He received the B.S. and M.S. in Physics from University of Bucharest, in 1995 and 1996, respectively, obtained his M.S. in Optics in 1999 and the Ph.D. in Optics in 2002 from CREOL. He did a postdoc at MIT, in Michael Feld's Lab. He authored a book on quantitative phase imaging (QPI), edited another book on NanoBiophotonics, authored 115 journal publications, 160 conference presentations, 30 patents, and gave 140 invited talks. He founded Phi Optics, Inc., a start-up company that commercializes QPI technology. He is an OSA and SPIE Fellow.

Refernces

[1] W. L. Bragg, The structure of some crystals as indicated by their diffraction of x-rays. P R Soc Lond a-Conta **89**(610), 248–277 (1913).
[2] J. Als-Nielsen and D. McMorrow, Elements of Modern X-Ray Physics (Wiley, New York, 2001) pp xi, 318.
[3] A. C. Kak and M. Slaney, Principles of Computerized Tomographic Imaging (Society for Industrial and Applied Mathematics, Philadelphia, 2001) pp xiv, 327.
[4] E. Wolf, History and solution of the phase problem in the theory of structure determination of crystals from X-ray diffraction measurements. Adv Imag Elect Phys **165**, 283–325 (2011).
[5] E. Wolf, Three-dimensional structure determination of semi-transparent objects from holographic data. Opt Commun **1**(4), 153 (1969).
[6] R. Fiolka, K. Wicker, R. Heintzmann, and A. Stemmer, Simplified approach to diffraction tomography in optical microscopy. Optics Express **17**(15), 12407–12417 (2009).
[7] O. Haeberle, K. Belkebir, H. Giovaninni, and A. Sentenac, Tomographic diffractive microscopy: basics, techniques and perspectives. Journal of Modern Optics **57**(9), 686–699 (2010).
[8] W. Choi, et al. Tomographic phase microscopy. Nature Methods **4**(9), 717–719 (2007).
[9] Y. Sung, W. Choi, N. Lue, R. R. Dasari, and Z. Yaqoob, Stain-free quantification of chromosomes in live cells using regularized tomographic phase microscopy. Plos One **7**(11), e49502 (2012).
[10] F. Charriere, et al. Cell refractive index tomography by digital holographic microscopy. Opt. Lett. **31**(2), 178–180 (2006).
[11] J. W. Goodman Speckle Phenomena in Optics: Theory and Applications (Roberts & Co, 2007).
[12] Y. Cotte, et al. Marker-free phase nanoscopy. Nature Photon. **7**(2), 113–117 (2013).
[13] D. Huang, et al. Optical coherence tomography. Science **254**(5035), 1178–1181 (1991).
[14] T. S. Ralston, D. L. Marks, P. S. Carney, and S. A. Boppart, Interferometric synthetic aperture microscopy. Nat Phys **3**(2), 129–134 (2007).
[15] A. F. Fercher, W. Drexler, C. K. Hitzenberger, and T. Lasser, Optical coherence tomography - principles and applications. Rep Prog Phys **66**(2), 239–303 (2003).
[16] A. F. Fercher, Optical coherence tomography. Journal of Biomedical Optics **1**(2), 157–173 (1996).
[17] T. S. Ralston, D. L. Marks, P. S. Carney, and S. A. Boppart, Real-time interferometric synthetic aperture microscopy. Optics Express **16**(4), 2555–2569 (2008).
[18] T. S. Ralston, D. L. Marks, S. A. Boppart, and P. S. Carney, Inverse scattering for high-resolution interferometric microscopy. Optics Letters **31**(24), 3585–3587 (2006).
[19] G. Popescu, Quantitative Phase Imaging of Cells and Tissues (McGraw Hill, 2011).
[20] D. Gabor, A new microscopic principle. Nature **161**, 777 (1948).
[21] F. Zernike, Phase contrast, a new method for the microscopic observation of transparent objects, Part 1. Physica **9**(7), 686–698 (1942).
[22] F. Zernike, Phase contrast, a new method for the microscopic observation of transparent objects, Part 2. Physica **9**, 974–986 (1942).
[23] H. F. Ding, et al. Fourier Transform Light Scattering (FTLS) of Cells and Tissues. J Comput Theor Nanos **7**(12), 2501–2511 (2010).
[24] S. A. Alexandrov and D. D. Sampson, Spatial information transmission beyond a system's diffraction limit using optical spectral encoding of the spatial frequency. J Opt a-Pure Appl Op **10**(2), 025304 (2008).
[25] S. A. Alexandrov, T. R. Hillman, T. Gutzler, and D. D. Sampson, Synthetic aperture fourier holographic optical microscopy. Physical Review Letters **97**(16), 168102 (2006).
[26] Z. Wang, et al. Spatial light interference tomography (SLIT). Opt Express **19**(21), 19907–19918 (2011).

[27] M. Mir, et al. Visualizing Escherichia coli Sub-Cellular Structure Using Sparse Deconvolution Spatial Light Interference Tomography. PLoS ONE **7**(6), e39816 (2012).
[28] H. F. Ding, Z. Wang, F. Nguyen, S. A. Boppart, and G. Popescu, Fourier Transform Light Scattering of Inhomogeneous and Dynamic Structures. Physical Review Letters **101**(23), 238102 (2008).
[29] T. Kim, et al. White-light diffraction tomography of unlabelled live cells. Nat Photon **8**(3), 256–263 (2014).
[30] A. Sentenac, P. C. Chaumet, and K. Belkebir, Beyond the Rayleigh criterion: Grating assisted far-field optical diffraction tomography. Physical Review Letters **97**(24) (2006).
[31] A. Wax, C. Yang, R. R. Dasari, and M. S. Feld, Angular light scattering studies using low-coherence interferometry. Proc. SPIE **4251**, 32–42 (2001).
[32] A. Wax, C. Yang, R. R. Dasari, and M. S. Feld, Measurement of angular distributions by use of low-coherence interferometry for light-scattering spectroscopy. Optics Letters **26**(6), 322–324 (2001).
[33] A. Wax, et al. Determination of particle size by using the angular distribution of backscattered light as measured with low-coherence interferometry. J Opt Soc Am A **19**(4), 737–744 (2002).
[34] S. A. Alexandrov, T. R. Hillman, and D. D. Sampson, Spatially resolved Fourier holographic light scattering angular spectroscopy. Optics Letters **30**(24), 3305–3307 (2005).
[35] T. Kim, S. Sridharan, and G. Popescu. Fourier Transform Light Scattering of Tissues. Handbook of Coherent-Domain Optical Methods, 2 Ed Vol **1**, ed. V. V. Tuchin (Springer, New York, 2013) pp 259–290.
[36] G. Popescu, T. Ikeda, R. R. Dasari, and M. S. Feld, Diffraction phase microscopy for quantifying cell structure and dynamics. Opt Lett **31**(6), 775–777 (2006).
[37] Z. Wang and G. Popescu, Quantitative phase imaging with broadband fields. Appl Phys Lett **96**, 051117 (2010).
[38] Z. Wang, H. Ding, and G. Popescu, Scattering-phase theorem. Optics Letters **36**, 1215 (2011).
[39] H. Ding, Z. Wang, X. Liang, S. A. Boppart, and G. Popescu, Measuring the scattering parameters of tissues from quantitative phase imaging of thin slices. Optics Letters **36**, 2281 (2011).
[40] R. Wang, et al. Dispersion-relation phase spectroscopy of intracellular transport. Opt Express **19**(21), 20571–20579 (2011).
[41] R. Wang, et al. One-dimensional deterministic transport in neurons measured by dispersion-relation phase spectroscopy. J. Phys.: Cond. Matter **23**, 374107 (2011).
[42] F. Charriere, et al. Living specimen tomography by digital holographic microscopy: morphometry of testate amoeba. Opt Express **14**(16), 7005–7013 (2006).
[43] Y. J. Sung, et al. Optical diffraction tomography for high resolution live cell imaging. Opt Express **17**(1), 266–277 (2009).
[44] Z. Wang, et al. Spatial light interference microscopy (SLIM). Opt Express **19**(2), 1016 (2011).
[45] R. Zhou, T. Kim, L. L. Goddard, and G. Popescu, Inverse scattering solutions using low-coherence light. Optics Letters **39**(15), 4494–4497 (2014).
[46] M. Mir, B. Bhaduri, R. Wang, R. Y. Zhu, and G. Popescu, Quantitative Phase Imaging. Prog Optics **57**, 133–217 (2012).
[47] D. Zicha, E. Genot, G. A. Dunn, and I. M. Kramer, TGF beta 1 induces a cell-cycle-dependent increase in motility of epithelial cells. J. Cell Sci. **112**(4), 447–454 (1999).
[48] G. A. Dunn, D. Zicha, and P. E. Fraylich, Rapid, microtubule-dependent fluctuations of the cell margin. J. Cell Sci. **110**, 3091–3098 (1997).
[49] B. Joshi, et al. Label-free route to rapid, nanoscale characterization of cellular structure and dynamics through opaque media. Scientific reports **3**, 2822 (2013).
[50] B. Bhaduri, et al. Cardiomyocyte imaging using real-time spatial light interference microscopy (SLIM). PLoS ONE **8**(2), e56930 (2013).
[51] Y. K. Park, et al. Refractive index maps and membrane dynamics of human red blood cells parasitized by Plasmodium falciparum. Proceedings of the National Academy of Sciences of the United States of America **105**, 13730 (2008).
[52] P. Bon, J. Savatier, M. Merlin, B. Wattellier, and S. Monneret, Optical detection and measurement of living cell morphometric features with single-shot quantitative phase microscopy. Journal of Biomedical Optics **17**(7), 076004 (2012).
[53] Y. Park, et al. Measurement of red blood cell mechanics during morphological changes. Proc Natl Acad Sci U S A **107**(15), 6731–6736 (2010).
[54] D. Zicha and G. A. Dunn, An Image-Processing System For Cell Behavior Studies In Subconfluent Cultures. J. Microscopy **179**, 11–21 (1995).
[55] G. Popescu, et al. Optical imaging of cell mass and growth dynamics. Am J Physiol-Cell Ph **295**(2), C538-C544 (2008).
[56] M. Mir, K. Tangella, and G. Popescu, Blood testing at the single cell level using quantitative phase and amplitude microscopy. Biomedical optics express **2**(12), 3259–3266 (2011).
[57] Y. Sung, et al. Size homeostasis in adherent cells studied by synthetic phase microscopy. Proceedings of the National Academy of Sciences **110**(41), 16687–16692 (2013).
[58] S. Sridharan, M. Mir, and G. Popescu, Simultaneous optical measurements of cell motility and growth. Biomedical optics express **2**(10), 2815–2820 (2011).
[59] G. Popescu, et al. Erythrocyte structure and dynamics quantified by Hilbert phase microscopy. J Biomed Opt **10**(6), 060503 (2005).
[60] G. Popescu, et al. Fourier phase microscopy for investigation of biological structures and dynamics. Optics letters **29**(21), 2503–2505 (2004).
[61] H. V. Pham, B. Bhaduri, K. Tangella, C. Best-Popescu, and G. Popescu, Real time blood testing using quantitative phase imaging. PLoS One **8**(2), e55676 (2013).
[62] R. Wang, H. Ding, M. Mir, K. Tangella, and G. Popescu, Effective 3D viscoelasticity of red blood cells measured by diffraction phase microscopy. Biomedical Optics Express **2**(3), 485–490 (2011).
[63] Y. Park, C. A. Best-Popescu, R. R. Dasari, and G. Popescu, Light scattering of human red blood cells during metabolic

remodeling of the membrane. Journal of Biomedical Optics **16**(1), 011013 (2011).

[64] J. Lim, et al. Born approximation model for light scattering by red blood cells. Biomedical Optics Express **2**(10), 2784–2791 (2011).

[65] E. Ben-Isaac, et al. Effective Temperature of Red-Blood-Cell Membrane Fluctuations. Physical Review Letters **106**(23), 238103 (2011).

[66] M. Mir, et al. Blood screening using diffraction phase cytometry. Journal of Biomedical Optics **15**(2), 027016 (2010).

[67] M. Mir, Z. Wang, K. Tangella, and G. Popescu, Diffraction Phase Cytometry: blood on a CD-ROM. Opt Express **17**(4), 2579–2585 (2009).

[68] G. Popescu, et al. Imaging red blood cell dynamics by quantitative phase microscopy. Blood cells, molecules & diseases **41**(1), 10–16 (2008).

[69] G. Popescu, Y. Park, R. R. Dasari, K. Badizadegan, and M. S. Feld, Coherence properties of red blood cell membrane motions. Physical review. E, Statistical, nonlinear, and soft matter physics **76**(3 Pt 1), 031902 (2007).

[70] M. S. Amin, et al. Microrheology of red blood cell membranes using dynamic scattering microscopy. Opt. Express. **15**, 17001 (2007).

[71] G. Popescu, K. Badizadegan, R. R. Dasari, and M. S. Feld, Observation of dynamic subdomains in red blood cells. J. Biomed. Opt. Lett. **11**, 040503 (2006).

[72] T. Ikeda, G. Popescu, R. R. Dasari, and M. S. Feld, Hilbert phase microscopy for investigating fast dynamics in transparent systems. Opt. Lett. **30**(10), 1165–1168 (2005).

[73] C. M. Joo and J. F. de Boer, Spectral-domain optical coherence reflectometric sensor for highly sensitive molecular detection. Optics Letters **32**(16), 2426–2428 (2007).

[74] M. A. Choma, A. K. Ellerbee, S. Yazdanfar, and J. A. Izatt, Doppler flow imaging of cytoplasmic streaming using spectral domain phase microscopy. Journal of Biomedical Optics **11**(2), - (2006).

[75] M. A. Choma, A. K. Ellerbee, C. H. Yang, T. L. Creazzo, and J. A. Izatt, Spectral-domain phase microscopy. Opt. Lett. **30**(10), 1162–1164 (2005).

[76] B. Rappaz, et al. Measurement of the integral refractive index and dynamic cell morphometry of living cells with digital holographic microscopy. Opt. Exp. **13**(23), 9361–9373 (2005).

[77] T. Akkin, C. Joo, and J. F. de Boer, Depth-resolved measurement of transient structural changes during action potential propagation. Biophysical Journal **93**(4), 1347–1353 (2007).

[78] T. Akkin, D. P. Dave, T. E. Milner, and H. G. Rylander, Detection of neural activity using phase-sensitive optical low-coherence reflectometry. Opt. Express **12**(11), 2377–2386 (2004).

[79] C. Fang-Yen, M. C. Chu, H. S. Seung, R. R. Dasari, and M. S. Feld, Noncontact measurement of nerve displacement during action potential with a dual-beam low-coherence interferometer. Opt. Lett. **29**(17), 2028–2030 (2004).

[80] N. Lue, et al. Live cell refractometry using microfluidic devices. Opt. Lett. **31**, 2759 (2006).

[81] N. Lue, et al. Tissue refractometry using Hilbert phase microscopy. Opt. Lett. **32**, 3522 (2007).

[82] E. J. McDowell, A. K. Ellerbee, M. A. Choma, B. E. Applegate, and J. A. Izatt, Spectral domain phase microscopy for local measurements of cytoskeletal rheology in single cells. J Biomed Opt **12**(4), 044008 (2007).

[83] Y. K. Park, G. Popescu, R. R. Dasari, K. Badizadegan, and M. S. Feld, Fresnel particle tracking in three dimensions using diffraction phase microscopy. Opt. Lett. **32**, 811 (2007).

[84] N. Lue, et al. Synthetic aperture tomographic phase microscopy for 3D imaging of live cells in translational motion. Opt Express **16**(20), 16240–16246 (2008).

[85] T. Kim, R. Zhou, L. L. Goddard, and G. Popescu, Breakthroughs in Photonics 2013: Quantitative Phase Imaging: Metrology Meets Biology. IEEE Photonics J **6**(2) (2014).

[86] B. Bhaduri, et al. Diffraction phase microscopy: principles and applications in materials and life sciences. Adv Opt Photonics **6**(1), 57–119 (2014).

[87] U. Schnars and W. Juptner, Direct Recording of Holograms by a Ccd Target and Numerical Reconstruction. Appl Optics **33**(2), 179–181 (1994).

[88] P. Marquet, et al. Digital holographic microscopy: a noninvasive contrast imaging technique allowing quantitative visualization of living cells with subwavelength axial accuracy. Opt. Lett. **30**(5), 468–470 (2005).

[89] E. Cuche, P. Marquet, and C. Depeursinge, Simultaneous amplitude-contrast and quantitative phase-contrast microscopy by numerical reconstruction of Fresnel off-axis holograms. Appl Optics **38**(34), 6994–7001 (1999).

[90] I. Yamaguchi and T. Zhang, Phase-shifting digital holography. Optics Letters **22**(16), 1268–1270 (1997).

[91] T. Zhang and I. Yamaguchi, Three-dimensional microscopy with phase-shifting digital holography. Optics Letters **23**(15), 1221–1223 (1998).

[92] G. Coppola, et al. A digital holographic microscope for complete characterization of microelectromechanical systems. Measurement Science & Technology **15**(3), 529–539 (2004).

[93] C. Edwards, A. Arbabi, G. Popescu, and L. L. Goddard, Optically monitoring and controlling nanoscale topography during semiconductor etching. Light Sci Appl **1**:e30 (2012).

[94] R. Zhou, C. Edwards, A. Arbabi, G. Popescu, and L. L. Goddard, Detecting 20 nm Wide Defects in Large Area Nanopatterns Using Optical Interferometric Microscopy. Nano Lett **13**(8), 3716–3721 (2013).

[95] G. Rajshekhar, et al. Nanoscale topography and spatial light modulator characterization using wide-field quantitative phase imaging. Optics Express **22**(3), 3432–3438 (2014).

[96] C. Edwards, et al. Diffraction phase microscopy: monitoring nanoscale dynamics in materials science [Invited]. Applied Optics **53**(27), G33-G43 (2014).

[97] C. Edwards, S. J. McKeown, J. Zhou, G. Popescu, and L. L. Goddard, In situ measurements of the axial expansion of palladium microdisks during hydrogen exposure using diffraction phase microscopy. Opt. Mater. Express **4**(12), 2559–2564 (2014).

[98] F. Charrière, et al. Characterization of microlenses by digital holographic microscopy. Applied Optics **45**(5), 829–835 (2006).

[99] T. Colomb, et al. Digital holographic reflectometry. Optics Express **18**(4), 3719–3731 (2010).
[100] C. J. Mann, P. R. Bingham, V. C. Paquit, and K. W. Tobin, Quantitative phase imaging by three-wavelength digital holography. Optics Express **16**(13), 9753–9764 (2008).
[101] M. T. Rinehart, N. T. Shaked, N. J. Jenness, R. L. Clark, and A. Wax, Simultaneous two-wavelength transmission quantitative phase microscopy with a color camera. Optics Letters **35**(15), 2612–2614 (2010).
[102] M. Takeda, H. Ina, and S. Kobayashi, Fourier-Transform Method of Fringe-Pattern Analysis for Computer-Based Topography and Interferometry. JOSA **72**(1), 156–160 (1982).
[103] J. W. Goodman and R. W. Lawrence, Digital Image Formation from Electronically Detected Holograms. Applied Physics Letters **11**(3), 77 (1967).
[104] E. Cuche, F. Bevilacqua, and C. Depeursinge, Digital holography for quantitative phase-contrast imaging. Optics Letters **24**(5), 291–293 (1999).
[105] D. Carl, B. Kemper, G. Wernicke, and G. von Bally, Parameter-optimized digital holographic microscope for high-resolution living-cell analysis. Appl Optics **43**(36), 6536–6544 (2004).
[106] B. Kemper, et al. Investigation of living pancreas tumor cells by digital holographic microscopy. J Biomed Opt **11**(3), 34005 (2006).
[107] P. Ferraro, S. De Nicola, A. Finizio, G. Pierattini, and G. Coppola, Recovering image resolution in reconstructing digital off-axis holograms by Fresnel-transform method. Applied Physics Letters **85**(14), 2709–2711 (2004).
[108] G. Popescu, et al. Optical measurement of cell membrane tension. Phys Rev Lett **97**(21), 218101 (2006).
[109] N. Lue, et al. Live Cell Refractometry Using Hilbert Phase Microscopy and Confocal Reflectance Microscopy. Journal of Physical Chemistry A **113**(47), 13327–13330 (2009).
[110] G. A. Dunn and D. Zicha, Phase-Shifting Interference Microscopy Applied to the Analysis of Cell Behavior. Sym Soc Exp Biol **47**, 91–106 (1993).
[111] G. A. Dunn and D. Zicha, Dynamics of Fibroblast Spreading. J Cell Sci **108**, 1239–1249 (1995).
[112] D. O. Hogenboom and C. A. DiMarzio, Quadrature detection of a Doppler signal. Applied Optics **37**(13), 2569–2572 (1998).
[113] D. O. Hogenboom, C. A. DiMarzio, T. J. Gaudette, A. J. Devaney, and S. C. Lindberg, Three-dimensional images generated by quadrature interferometry. Optics Letters **23**(10), 783–785 (1998).
[114] W. C. Warger, J. A. Newmark, C. M. Warner, and C. A. DiMarzio, Phase-subtraction cell-counting method for live mouse embryos beyond the eight-cell stage. Journal of Biomedical Optics **13**(3), 034005–034001 (2008).
[115] N. Warnasooriya, et al. Imaging gold nanoparticles in living cell environments using heterodyne digital holographic microscopy. Opt Express **18**(4), 3264–3273 (2010).
[116] J. E. Millerd, et al. Pixelated phase-mask dynamic interferometer. Proc. SPIE **5531**, 304–314 (2004).
[117] W. C. Warger and C. A. DiMarzio, Computational signal-to-noise ratio analysis for optical quadrature microscopy. Opt Express **17**(4), 2400–2422 (2009).
[118] M. Novak, et al. Analysis of a micropolarizer array-based simultaneous phase-shifting interferometer. Appl Optics **44**(32), 6861–6868 (2005).
[119] T. Tahara, et al. Single-shot polarization-imaging digital holography based on simultaneous phase-shifting interferometry. Optics Letters **36**(16), 3254–3256 (2011).
[120] B. Bhaduri, K. Tangella, and G. Popescu, Fourier phase microscopy with white light. Biomedical Optics Express **4**(8), 1434–1441 (2013).
[121] Y. K. Park, G. Popescu, K. Badizadegan, R. R. Dasari, and M. S. Feld, Diffraction phase and fluorescence microscopy. Optics Express **14**(18), 8263–8268 (2006).
[122] B. Bhaduri, H. Pham, M. Mir, and G. Popescu, Diffraction phase microscopy with white light. Optics Letters **37**(6), 1094–1096 (2012).
[123] V. Mico, Z. Zalevsky, and J. Garcia, Superresolution optical system by common-path interferometry. Optics Express **14**(12), 5168–5177 (2006).
[124] V. Mico, C. Ferreira, Z. Zalevsky, and J. Garcia, Spatially-multiplexed interferometric microscopy (SMIM), converting a standard microscope into a holographic one. Optics Express **22**(12), 14929–14943 (2014).
[125] P. Bon, G. Maucort, B. Wattellier, and S. Monneret, Quadriwave lateral shearing interferometry for quantitative phase microscopy of living cells. Optics Express **17**(15), 13080–13094 (2009).
[126] S. Bernet, A. Jesacher, S. Furhapter, C. Maurer, and M. Ritsch-Marte, Quantitative imaging of complex samples by spiral phase contrast microscopy. Opt Express **14**(9), 3792–3805 (2006).
[127] S. S. Kou, L. Waller, G. Barbastathis, and C. J. R. Sheppard, Transport-of-intensity approach to differential interference contrast (TI-DIC) microscopy for quantitative phase imaging. Optics Letters **35**(3), 447–449 (2010).
[128] L. Waller, L. Tian, and G. Barbastathis, Transport of Intensity phase-amplitude imaging with higher order intensity derivatives. Optics Express **18**(12), 12552–12560 (2010).
[129] D. Paganin and K. A. Nugent, Noninterferometric Phase Imaging with Partially Coherent Light. Physical Review Letters **80**(12), 2586–2589 (1998).
[130] A. Barty, K. A. Nugent, D. Paganin, and A. Roberts, Quantitative optical phase microscopy. Optics Letters **23**(11), 817–819 (1998).
[131] G. Zheng, R. Horstmeyer, and C. Yang, Wide-field, high-resolution Fourier ptychographic microscopy. Nat Photon **7**(9), 739–745 (2013).
[132] R. W. Gerchberg, A practical algorithm for the determination of phase from image and diffraction plane pictures. Optik **35**(2), 237–246 (1972).
[133] J. R. Fienup, Phase retrieval algorithms: a comparison. Applied Optics **21**(15), 2758–2769 (1982).
[134] H. V. Pham, C. Edwards, L. L. Goddard, and G. Popescu, Fast phase reconstruction in white light diffraction phase microscopy. Applied Optics **52**(1), A97–A101 (2013).
[135] C. Edwards, et al. The effects of spatial coherence in diffraction phase microscopy. Opt. Exp. **22**(5), 5133–5146 (2014).
[136] T. H. Nguyen, C. Edwards, L. L. Goddard, and G. Popescu, Quantitative phase imaging with partially coherent illumination. Optics Letters **39**(19), 5511–5514 (2014).

[137] S. D. Babacan, Z. Wang, M. Do, and G. Popescu, Cell imaging beyond the diffraction limit using sparse deconvolution spatial light interference microscopy. Biomedical Optics Express **2**(7), 1815–1827 (2011).
[138] M. Mir, et al. Optical measurement of cycle-dependent cell growth. Proceedings of the National Academy of Sciences **108**(32), 13124–13129 (2011).
[139] M. Mir, et al. Label-free characterization of emerging human neuronal networks. Sci Rep **4**, 4434 (2014).
[140] W. C. Warger Ii and C. A. DiMarzio, Computational signal-to-noise ratio analysis for optical quadrature microscopy. Optics Express **17**(4), 2400–2422 (2009).
[141] A. P. Y. Wong and P. Wiltzius, Dynamic Light-Scattering with a Ccd Camera. Review of Scientific Instruments **64**(9), 2547–2549 (1993).
[142] F. Scheffold and R. Cerbino, New trends in light scattering. Current Opinion in Colloid & Interface Science **12**(1), 50–57 (2007).
[143] R. Dzakpasu and D. Axelrod, Dynamic light scattering microscopy. A novel optical technique to image submicroscopic motions. II: Experimental applications. Biophysical Journal **87**(2), 1288–1297 (2004).
[144] J. Neukammer, C. Gohlke, A. Hope, T. Wessel, and H. Rinneberg, Angular distribution of light scattered by single biological cells and oriented particle agglomerates. Appl Optics **42**(31), 6388–6397 (2003).
[145] W. Choi, et al. Field-based angle-resolved light-scattering study of single live cells. Optics Letters **33**(14), 1596–1598 (2008).
[146] J. W. Pyhtila and A. Wax, Rapid, depth-resolved light scattering measurements using Fourier domain, angle-resolved low coherence interferometry. Optics Express **12**(25), 6178–6183 (2004).
[147] K. J. Chalut, et al. Label-Free, High-Throughput Measurements of Dynamic Changes in Cell Nuclei Using Angle-Resolved Low Coherence Interferometry. Biophysical Journal **94**(12), 4948–4956 (2008).
[148] M. G. Giacomelli, K. J. Chalut, J. H. Ostrander, and A. Wax, Application of the T-matrix method to determine the structure of spheroidal cell nuclei with angle-resolved light scattering. Optics Letters **33**(21), 2452–2454 (2008).
[149] C. Amoozegar, M. G. Giacomelli, J. D. Keener, K. J. Chalut, and A. Wax, Experimental verification of T-matrix-based inverse light scattering analysis for assessing structure of spheroids as models of cell nuclei. Applied Optics **48**(10), D20–D25 (2009).
[150] F. E. Robles and A. Wax, Measuring morphological features using light-scattering spectroscopy and Fourier-domain low-coherence interferometry. Optics Letters **35**(3), 360–362 (2010).
[151] N. Terry, et al. Detection of intestinal dysplasia using angle-resolved low coherence interferometry. Journal of Biomedical Optics **16**(10), 106002–106006 (2011).
[152] Y. Zhu, N. G. Terry, and A. Wax, Scanning fiber angle-resolved low coherence interferometry. Optics Letters **34**(20), 3196–3198 (2009).
[153] Y. Zhu, N. G. Terry, J. T. Woosley, N. J. Shaheen, and A. Wax, Design and validation of an angle-resolved low-coherence interferometry fiber probe for in vivo clinical measurements of depth-resolved nuclear morphology. J Biomed Opt **16**(1), 011003 (2011).
[154] N. G. Terry, et al. Detection of Dysplasia in Barrett's Esophagus With In Vivo Depth-Resolved Nuclear Morphology Measurements. Gastroenterology **140**(1), 42–50 (2011).
[155] H. Ding, F. Nguyen, S. A. Boppart, and G. Popescu, Optical properties of tissues quantified by Fourier transform light scattering. Opt. Lett. **34**, 1372 (2009).
[156] F. Brochard and J. F. Lennon, Frequency Spectrum of Flicker Phenomenon in Erythrocytes. Journal De Physique **36**(11), 1035–1047 (1975).
[157] H. Ding, L. J. Millet, M. U. Gillette, and G. Popescu, Actin-driven cell dynamics probed by Fourier transform light scattering. Biomed. Opt. Express **1**, 260 (2010).
[158] H. F. Ding, et al. Fourier Transform Light Scattering of Biological Structure and Dynamics. Ieee J Sel Top Quant **16**(4), 909–918 (2010).
[159] Y. Jo, et al. Angle-resolved light scattering of individual rod-shaped bacteria based on Fourier transform light scattering. Sci. Rep. **4** (2014).
[160] Y. Kim, J. M. Higgins, R. R. Dasari, S. Suresh, and Y. Park, Anisotropic light scattering of individual sickle red blood cells. Journal of Biomedical Optics **17**(4), 0405011–0405013 (2012).
[161] H. Yu, H. Park, Y. Kim, M. W. Kim, and Y. Park, Fourier-transform light scattering of individual colloidal clusters. Optics Letters **37**(13), 2577–2579 (2012).
[162] J. Jung and Y. Park, Spectro-angular light scattering measurements of individual microscopic objects. Optics Express **22**(4), 4108–4114 (2014).
[163] K. Kim and Y. Park, Fourier transform light scattering angular spectroscopy using digital inline holography. Optics Letters **37**(19), 4161–4163 (2012).
[164] K. Lee, et al. Synthetic Fourier transform light scattering. Optics Express **21**(19), 22453–22463 (2013).
[165] W. Oldendorf, Isolated flying spot detection of radiodensity discontinuities - displaying internal structural pattern of a complex object. Ire T Biomed Electr **Bme8**(1), 68-& (1961).
[166] H. Hornich, A tribute to Radon, Johann. Ieee T Med Imaging **5**(4), 169–169 (1986).
[167] R. Snyder and L. Hesselink, High-Speed Optical Tomography for Flow Visualization. Appl Optics **24**(23), 4046–4051 (1985).
[168] K. Bennett and R. L. Byer, Optical tomography - experimental-verification of noise theory. Optics Letters **9**(7), 270–272 (1984).
[169] A. Schatzberg and A. J. Devaney, Rough-Surface Inverse Scattering within the Rytov Approximation. J Opt Soc Am A **10**(5), 942–950 (1993).
[170] A. J. Devaney, Inverse-scattering theory within the rytov approximation. Optics Letters **6**(8), 374–376 (1981).
[171] W. C. Chew Waves and fields in inhomogeneous media. (IEEE Press, New York) p xx, 608 (1995).
[172] T. Kim, et al. Deterministic signal associated with a random field. Optics Express **21**(18), 20806–20820 (2013).
[173] Y. Yasuno, et al. Non-iterative numerical method for laterally superresolving Fourier domain optical coherence tomography. Optics Express **14**(3), 1006–1020 (2006).

[174] M. Ronne, Chromosome Preparation and High-Resolution Banding Techniques - a Review. J Dairy Sci **72**(5), 1363–1377 (1989).
[175] K. Kim, et al. High-resolution three-dimensional imaging of red blood cells parasitized by Plasmodium falciparum and in situ hemozoin crystals using optical diffraction tomography. Journal of Biomedical Optics **19**(1), 011005–011005 (2013).
[176] J. Girard, et al. Nanometric resolution using far-field optical tomographic microscopy in the multiple scattering regime. Phys Rev A **82**(6) (2010).
[177] E. Mudry, et al. Structured illumination microscopy using unknown speckle patterns. Nat Photonics **6**(5), 312–315 (2012).
[178] U. S. Kamilov, et al. Learning approach to optical tomography. Optica **2**(6), 517–522 (2015).
[179] R. Oldenbourg, A new view on polarization microscopy. Nature **381**(6585), 811–812 (1996).
[180] Z. Wang, L. J. Millet, M. U. Gillette, and G. Popescu, Jones phase microscopy of transparent and anisotropic samples. Optics Letters **33**(11), 1270–1272 (2008).
[181] V. Lauer, New approach to optical diffraction tomography yielding a vector equation of diffraction tomography and a novel tomographic microscope. Journal of Microscopy-Oxford **205**, 165–176 (2002).
[182] T. Zhang, et al. Full-polarized Tomographic Diffraction Microscopy Achieves a Resolution about One-Fourth of the Wavelength. Physical Review Letters **111**(24) (2013).
[183] J. R. Fienup, Phase retrieval algorithms - a comparison. Appl Optics **21**(15), 2758–2769 (1982).
[184] N. Streibl, Phase imaging by the transport-equation of intensity. Opt Commun **49**(1), 6–10 (1984).
[185] G. A. Zheng, R. Horstmeyer, and C. H. Yang, Wide-field, high-resolution Fourier ptychographic microscopy. Nat Photonics **7**(9), 739–745 (2013).
[186] L. Tian and L. Waller, 3D intensity and phase imaging from light field measurements in an LED array microscope. Optica **2**(2), 104–111 (2015).
[187] L. Tian, X. Li, K. Ramchandran, and L. Waller, Multiplexed coded illumination for Fourier Ptychography with an LED array microscope. Biomedical Optics Express **5**(7), 2376–2389 (2014).
[188] L. Tian, et al. Compressive x-ray phase tomography based on the transport of intensity equation. Optics Letters **38**(17), 3418–3421 (2013).
[189] P. Hosseini, et al. Scanning color optical tomography (SCOT). Optics Express **23**(15), 19752–19762 (2015).
[190] W. D. Donachie, Co-ordinate regulation of the Escherichia coli cell cycle or The cloud of unknowing. Mol. Microbiol. **40**(4), 779–785 (2001).
[191] D. M. Raskin and P. A. J. De Boer, Rapid pole-to-pole oscillation of a protein required for directing division to the middle of Escherichia coli. Proc. Nat. Acad. Sci. **96**(9), 4971–4976 (1999).
[192] A. S. Ghosh and K. D. Young, Helical disposition of proteins and lipopolysaccharide in the outer membrane of Escherichia coli. J. Bacterio. **187**(6), 1913–1922 (2005).
[193] W. C. Lee, et al. Multivariate biophysical markers predictive of mesenchymal stromal cell multipotency. Proceedings of the National Academy of Sciences **111**(42), E4409–E4418 (2014).
[194] K. Jun Soo, P. Prabhakar, B. Vadim, and S. Igal, The influence of chromosome density variations on the increase in nuclear disorder strength in carcinogenesis. Physical Biology **8**(1), 015004 (2011).